

Structural Optimization Techniques Combined With Meshless Methods: A Review

ANTÓNIO PEDRO GONÇALVES DE CASTRO

junho de 2021

**COMBINING RADIAL POINT INTERPOLATION MESHLESS
METHODS WITH STRUCTURAL OPTIMIZATION
APPROACHES**

António Pedro Gonçalves de Castro
1150649

2021

Instituto Superior de Engenharia do Porto
Departamento de Engenharia Mecânica



POLITÉCNICO
DO PORTO

isep

COMBINING RADIAL POINT INTERPOLATION MESHLESS METHODS WITH STRUCTURAL OPTIMIZATION APPROACHES

António Pedro Gonçalves de Castro
1150649

Dissertation presented to the School of Engineering of the Polytechnic of Porto (ISEP) within the scope of the unit course “Research and Planning Methodologies” of the Master in Mechanical Engineering course, supervised by Professor Jorge Américo Oliveira Pinto Belinha.

2021

Instituto Superior de Engenharia do Porto
Departamento de Engenharia Mecânica



POLITÉCNICO
DO PORTO

isep

AGRADECIMENTOS

Primeiramente agradeço ao Engenheiro Jorge Belinha, por todo o apoio, disponibilidade e motivação ao longo da realização deste trabalho.

Aos meus amigos que sempre me ajudaram e me motivaram, quando tudo parecia estar a correr mal.

Por fim, aos meus pais e irmã, que sempre me apoiaram nas decisões que tomei, e que tornaram possível todo este percurso.

A todos, obrigado.

KEYWORDS

Structural optimization; Topology optimization; Meshless methods; Finite element method

ABSTRACT

Structural optimization has been growing in recent years, as it is an excellent tool to obtain reliable and high-performance products. In addition to reducing the waste of resources and emissions as well as the production cost, this can be applied in several areas from engineering to medicine.

The numerical method most used in recent decades to obtain structurally optimized parts is the finite element method (FEM) and it is included in the group called mesh-based methods. However, the application of these methods in parts with complex geometries and in large deformation problems result in low accuracy and instable solutions. In order to solve this problem, in the last decades, methods that are independent of a mesh have been developed to obtain unknown variables, called meshless methods. Although meshless methods are still recent and there are few documentations, these have been showing good results compared to the mesh-based methods, proving to be a good alternative.

Considering what has been said previously, this work has as main objective the study and analysis of parts subjected to structural optimization using mesh-based and meshless methods, in order to compare the results and verify the benefits of using a type of method instead of the other.

PALAVRAS CHAVE

Optimização estrutural; Optimização topológica; Métodos sem malha; Método dos Elementos Finitos

RESUMO

A optimização estrutural tem vindo a crescer nos últimos anos, uma vez que é uma excelente ferramenta para a obtenção de produtos fiáveis e de alto desempenho. Para além de que reduz o gasto de recursos e emissões assim como o preço de produção das mesmas, esta pode ser aplicada em diversas áreas desde a engenharia à medicina.

O método numérico mais utilizado nas últimas décadas para a obtenção de partes estruturalmente optimizadas é o método dos elementos finitos (MEF), o qual pode ser incluído no grupo denominado de métodos com malha. No entanto, a aplicação destes métodos em partes com geometrias complexas e em problemas com grandes deformações resultam em soluções com pouca precisão e de baixa estabilidade. De modo a solucionar este problema, nas últimas décadas, têm vindo a ser desenvolvidos métodos que são independentes de uma malha para a obtenção das variáveis desconhecidas, denominados de métodos sem malha. Apesar dos métodos sem malha ainda serem recentes e existir pouca documentação, estes têm vindo a mostrar bons resultados comparativamente aos métodos com malha provando ser uma boa alternativa.

Tendo em conta o referido anteriormente, este trabalho tem como objectivo principal o estudo e análise de partes submetidas a optimização estrutural utilizando métodos com malha e sem malha, de modo a comparar os resultados e verificar os benefícios da utilização de um tipo de método relativamente ao outro.

LIST OF SYMBOLS AND ABBREVIATIONS

List of abbreviations

| | |
|--------|---|
| 2D | Bidimensional |
| 3D | Tridimensional |
| AESO | Additive Evolutionary Structural Optimization |
| BEM | Boundary Element Method |
| BESO | Bi-directional Evolutionary Structural Optimization |
| CSRBF | Compactly Supported Radial Basis Function |
| DEM | Diffuse Element Method |
| DR | Decrease Ratio |
| EFGM | Element Free Galerkin Method |
| ESO | Evolutionary Structural Optimization |
| FEM | Finite Element Method |
| FEMAP | Finite Element Modelling And Postprocessing |
| FEMAS | Finite Element and Meshless Analysis Software |
| MLPG | Meshless Local Petrov-Galerkin |
| MLS | Moving Least Square |
| MQ-RBF | Multi-Quadratics Radial Basis Functions |
| NEM | Natural Element Method |
| NNRPIM | Natural Neighbour Radial Point Interpolation Method |
| PIM | Point Interpolation Method |
| RBFM | Radial Basis Function Method |
| RKPM | Reproducing Kernel Particle Method |
| RPIM | Radial Point Interpolation Method |
| SPH | Smoothed Particle Hydrodynamics |
| VM | Von Mises |

List of units

| | |
|------|--------|
| N | Newton |
| Pa | Pascal |
| m | Meter |
| s | Second |

List of symbols

| | |
|-------------------|-----------------------------------|
| A | Area |
| $\mathbf{a}(x_I)$ | RBF coefficients |
| \mathbf{B} | Deformability matrix |
| \mathbf{b} | Body force per unit volume vector |
| $\mathbf{b}(x_I)$ | PBF coefficients |
| \mathbf{c} | Material constitutive matrix |

| | |
|----------------------------|---|
| D | Size of the support-domain |
| d | Domain dimension |
| d_{Ii} | Distance between the field nodes and the interest point |
| E | Young's elastic modulus |
| F | Force |
| \mathbf{f}_b | Body force vector |
| \mathbf{f}_t | External force vector |
| \mathbf{H} | Interpolation matrix |
| K | Stiffness |
| \mathbf{K} | Global Stiffness matrix |
| \mathbf{L} | Differential operator matrix |
| M_{Ii} | Middle points |
| \mathbf{M} | Assembled moment matrix |
| m | Number of monomials in the polynomial basis |
| N | Normal reaction force |
| \mathbf{N} | Nodal set vector |
| n | Number of nodes inside the influence-domain |
| \mathbf{n} | Unit outward vector normal to the boundary of domain |
| n_I | Interest node |
| \mathbf{P} | Polynomial moment matrix |
| P_I | Vertex of the Voronoï cell |
| $\mathbf{p}(\mathbf{x}_I)$ | PBF vector |
| \mathbf{R} | RBF moment matrix |
| \mathbb{R}^d | d-dimensional real numbers set |
| $\mathbf{r}(\mathbf{x}_I)$ | RBF vector |
| \mathbf{s} | Compliance elasticity matrix for the general anisotropic material |
| $\bar{\mathbf{t}}$ | Traction on the natural boundary |
| $u(\mathbf{x}_i)$ | Nodal values |
| \mathbf{u}_s | Nodal values vector |
| $\bar{\mathbf{u}}$ | Prescribed displacement on the essential boundary |
| $u^h(\mathbf{x}_I)$ | Interpolation function |
| \mathbf{V} | Voronoï cells vector |
| V_i | Voronoï cell |
| V_f | Volume fraction |
| \hat{w}_I | Weight of the integration point |
| w_η, w_ξ | Gauss-Legendre quadrature weights for an isoparametric quadrilateral cell |
| \mathbf{X} | Nodal coordinates vector |
| \mathbf{x} | Cartesian coordinates of a point |
| \mathbf{x}_I | Interest point |
| δ_{ij} | Kronecker delta property |

| | |
|--|----------------------------------|
| c, p | MQ-RBF parameters |
| $\boldsymbol{\varepsilon}$ | Deformation vector |
| $\boldsymbol{\Lambda}$ | Cauchy stress tensor |
| ν | Poisson's ratio |
| $\boldsymbol{\varphi}(\boldsymbol{x}_I)$ | Interpolation vector |
| Ψ | Virtual work |
| Γ | Boundary domain |
| Γ_t | Natural boundary |
| Γ_u | Essential boundary |
| Ω | Solid domain |
| % | Percentage |
| $\ \cdot\ $ | Euclidean norm |
| : | Such that |
| \forall | For all |
| ∇ | Gradient operator |
| \in | Belonging to |
| \wedge | And |
| = | Equal |
| \neq | Different |
| < | Less than |
| \gg | Much greater than |
| \geq | Greater than or equal to |
| \subset | Subset |
| \cup | Union |
| \cap | Intersection |
| \emptyset | Empty set |
| \mathbb{R}^2 | Two-dimensional real numbers set |
| $\boldsymbol{\psi}_1(\boldsymbol{x}_I)$ | Byproduct vector |

FIGURES INDEX

| | |
|--|----|
| FIG. 1 - GENERAL GAUSSIAN INTEGRATION MESH..... | 29 |
| FIG. 2 - TRANSFORMATION OF THE INITIAL QUADRILATERAL INTO AN ISOPARAMETRIC SQUARE SHAPE (2 X 2 INTEGRATION POINTS PER INTEGRATION CELL) | 30 |
| FIG. 3 - GENERAL GAUSSIAN INTEGRATION MESH..... | 30 |
| FIG. 4 - FITTED GAUSSIAN MESH | 31 |
| FIG. 5 – A) VORONOĬ CELL AND THE INTERSECTION POINTS (PI_i); B) MIDDLE POINTS (M_i) AND THE GENERATED QUADRILATERALS; C) QUADRILATERAL $nMI_4PI_4MI_5$ | 32 |
| FIG. 6 - A) VORONOĬ CELL AND THE INTERSECTION POINTS (PI_i); B) MIDDLE POINTS (M_i) AND THE GENERATED TRIANGLES; C) TRIANGLE nPI_7MI_1 | 32 |
| FIG. 7 – TRIANGULAR AND QUADRILATERAL SHAPES AND THEIR RESPECTIVE INTEGRATION POINTS x_I USING THE GAUSS-LEGENDRE INTEGRATION SCHEME | 33 |
| FIG. 8 – A) INFLUENCE-DOMAINS WITH DIFFERENT SIZES AND SHAPES; B) EXAMPLE OF A BAD CHOICE IN THE SIZE OF THE INFLUENCE-DOMAIN | 34 |
| FIG. 9 – A) INITIAL NODAL SET OF POTENTIAL NEIGHBOUR NODES OF NODE n_0 ; B) FIRST TRIAL PLANE; C) SECOND TRIAL PLANE; D) FINAL TRIAL CELL CONTAINING JUST THE NATURAL NEIGHBOURS OF NODE n_0 ; E) NODE n_0 AND THE RESPECTIVE VORONOĬ CELL V_0 ; F) VORONOĬ DIAGRAM | 35 |
| FIG. 10 – A) FIRST DEGREE INFLUENCE-CELL; B) SECOND DEGREE INFLUENCE-CELL..... | 36 |
| FIG. 11 - CANTILEVER BEAM MODEL [18]..... | 44 |
| FIG. 12 - OPTIMIZATION RESULT OBTAINED USING EFGM [18]. | 44 |
| FIG. 13 - OPTIMIZATION RESULT USING FEM WITHOUT SENSITIVITY FILTERING (A) AND USING SENSITIVITY FILTERING (B) [18]...... | 44 |
| FIG. 14 - CONVERGENCE HISTORY OF THE CANTILEVER BEAM USING EFGM [18]..... | 44 |
| FIG. 15 - INFLUENCE OF THE INITIAL MATERIAL LAYOUT ((A) AND (C)) ON THE OPTIMIZED DESIGN OF A CANTILEVER BEAM ((B) AND (D)) WITH STRUCTURAL COMPLEXITY CONTROL [19]. | 45 |
| FIG. 16 - INFLUENCE OF THE NUMBER OF THE HOLES ON THE OPTIMIZED DESIGN OF A CANTILEVER BEAM. THE INITIAL DESIGN, OPTIMIZED DESIGN, AND EVOLUTION HISTORIES OF VOLUME FRACTION AND NORMALIZED COMPLIANCE OF THE BEAM ARE PLOTTED FROM LEFT TO RIGHT FOR FOUR DIFFERENT CASES (A)-(C), (D)-(F), (G)-(I), (J)-(L) [19]. | 46 |
| FIG. 17 - INFLUENCE OF THE HOLE SIZE ON THE OPTIMIZED DESIGN ON A CANTILEVER BEAM. (A) TWO INTERIOR HOLES ARE INCLUDED IN THE INITIAL DESIGN. IN THE OPTIMIZATION, EACH HOLE IS REQUIRED TO BE NOT SMALLER THAN 0 FOR (B), 1/20 FOR (C), AND 1/10 FOR (D) OF THE VOLUME OF THE DESIGN DOMAIN [19]...... | 46 |
| FIG. 18 - THREE-DIMENSIONAL CANTILEVER BEAM MODEL AND ITS LOAD AND DISPLACEMENT BOUNDARY CONDITIONS [23]. | 47 |
| FIG. 19 - OPTIMIZED RESULTS BASED ON FOUR UNIFORM STRUCTURED MESHES. ALL THE RESULTS ARE COLORED BY THE DISPLACEMENT FIELD IN THE y DIRECTION [23]..... | 47 |
| FIG. 20 - CANTILEVER BEAM MODEL. | 51 |
| FIG. 21 – CANTILEVER BEAM OPTIMIZED SHAPE OBTAINED FROM LITERATURE [29]. | 52 |

FIG. 22 – CANTILEVER BEAM REGULAR MESH USING 640 QUADRILATERAL ELEMENTS (A) AND 1280 TRIANGULAR ELEMENTS (B)..... 52

FIG. 23 – CANTILEVER BEAM REGULAR QUADRILATERAL MESH USING 693 NODES (A) AND 2665 NODES (B)..... 54

FIG. 24 – CANTILEVER BEAM COMPUTATIONAL TIME PER ITERATION USING A REGULAR QUADRILATERAL MESH OF 693 NODES, FEM, RPIM AND NNRPIM FOR DR OF 2% (A), 3% (B), 4% (C), 5% (D) AND 10% (E)..... 59

FIG. 25 - CANTILEVER BEAM COMPUTATIONAL TIME PER ITERATION USING A REGULAR QUADRILATERAL MESH OF 2665 NODES, FEM, RPIM AND NNRPIM FOR DR OF 2% (A), 3% (B), 4% (C), 5% (D) AND 10% (E)..... 60

FIG. 26 – CANTILEVER BEAM COMPUTATIONAL TIME PER DR USING A REGULAR QUADRILATERAL MESH OF 693 NODES (A) AND 2665 NODES (B), FOR SOLUTIONS THAT REACHED THE SHAPE REFERRED IN LITERATURE..... 61

FIG. 27 – CANTILEVER BEAM MODEL VARIANT..... 61

FIG. 28 – CANTILEVER BEAM VARIANT IRREGULAR MESH OF 1294 TRIANGULAR ELEMENTS (A) AND ITS OPTIMIZATION SOLUTION (B)..... 62

FIG. 29 – CANTILEVER BEAM VARIANT REGULAR MESH OF 1020 TRIANGULAR ELEMENTS..... 62

FIG. 30 – CANTILEVER BEAM VARIANT OPTIMIZED SOLUTIONS USING FEM (A), RPIM (B) AND NNRPIM (C) USING A REGULAR MESH OF 1020 TRIANGULAR ELEMENTS..... 62

FIG. 31 – SIMPLY SUPPORTED BEAM MODEL..... 63

FIG. 32 – SIMPLY SUPPORTED BEAM OPTIMIZED SHAPE OBTAINED FROM LITERATURE [30]..... 63

FIG. 33 – SIMPLY SUPPORTED BEAM REGULAR QUADRILATERAL MESH USING 1326 NODES (A) AND 5151 NODES (B). 64

FIG. 34 – SIMPLY SUPPORTED BEAM COMPUTATIONAL TIME PER ITERATION USING A REGULAR QUADRILATERAL MESH OF 1326 NODES, FEM, RPIM AND NNRPIM FOR DR OF 4% (A), 5% (B) AND 10% (C)..... 68

FIG. 35 - SIMPLY SUPPORTED BEAM COMPUTATIONAL TIME PER ITERATION USING A REGULAR QUADRILATERAL MESH OF 5151 NODES, FEM, RPIM AND NNRPIM FOR DR OF 4% (A), 5% (B) AND 10% (C)..... 69

FIG. 36 – SIMPLY SUPPORTED BEAM COMPUTATIONAL TIME PER DR USING A REGULAR QUADRILATERAL MESH OF 1326 NODES (A) AND 5151 NODES (B), FOR SOLUTIONS THAT REACHED THE SHAPE REFERRED IN LITERATURE..... 70

FIG. 37 – HANDBRAKE LEVER DIMENSIONS FROM A STANDARD ROAD CAR..... 71

FIG. 38 – HANDBRAKE LEVER 2D (A) AND 3D (B) MODEL. 72

FIG. 39 – ESSENTIAL AND NATURAL BOUNDARY CONDITIONS APPLIED TO THE HANDBRAKE LEVER..... 72

FIG. 40 - COMPUTATIONAL TIME PER ITERATION COMPARISON BETWEEN 2D AND 3D MODELS USING FEM, RPIM AND NNRPIM FOR A DR OF 5%..... 74

FIG. 41 – PROPOSED OPTIMAL DESIGN 1 (A) AND 2 (B)..... 75

TABLES INDEX

| | |
|--|----|
| TABLE 1 – CANTILEVER BEAM OPTIMIZED SOLUTIONS USING QUADRILATERAL AND TRIANGULAR ELEMENTS FOR DR OF 4%, 5% AND 10% | 53 |
| TABLE 2 – CANTILEVER BEAM STRUCTURAL OPTIMIZATION SOLUTIONS USING FEM, RPIM AND NNRPIM AND DR OF 2%, 3%, 4%, 5% AND 10% FOR A REGULAR QUADRILATERAL MESH OF 693 NODES. ... | 55 |
| TABLE 3 - CANTILEVER BEAM STRUCTURAL OPTIMIZATION SOLUTIONS USING FEM, RPIM AND NNRPIM AND DR OF 2%, 3%, 4%, 5% AND 10% FOR A REGULAR QUADRILATERAL MESH OF 2665 NODES. . | 56 |
| TABLE 4 – SUMMARY OF THE CANTILEVER BEAM OPTIMAL SOLUTIONS THAT REACHED THE SHAPE REFERRED IN LITERATURE | 57 |
| TABLE 5 – SIMPLY SUPPORTED BEAM STRUCTURAL OPTIMIZATION SOLUTIONS USING FEM, RPIM AND NNRPIM AND DR OF 4%, 5% AND 10% FOR A REGULAR QUADRILATERAL MESH OF 1326 NODES. 65 | |
| TABLE 6 - SIMPLY SUPPORTED BEAM STRUCTURAL OPTIMIZATION SOLUTIONS USING FEM, RPIM AND NNRPIM AND DR OF 4%, 5% AND 10% FOR A REGULAR QUADRILATERAL MESH OF 5151 NODES. 66 | |
| TABLE 7 - SUMMARY OF THE SIMPLY SUPPORTED BEAM OPTIMAL SOLUTIONS THAT REACHED THE SHAPE REFERRED IN LITERATURE | 67 |
| TABLE 8 – HANDBRAKE LEVER 2D MODEL STRUCTURAL OPTIMIZATION SOLUTIONS USING FEM, RPIM AND NNRPIM AND DR OF 4%, 5% AND 10% FOR A MESH OF 1828 TRIANGULAR ELEMENTS. | 73 |
| TABLE 9 - HANDBRAKE LEVER 3D MODEL STRUCTURAL OPTIMIZATION SOLUTIONS USING FEM, RPIM AND NNRPIM AND DR OF 5% FOR A MESH OF 15397 TETRAHEDRAL ELEMENTS. | 74 |
| TABLE 10 – DISPLACEMENT AND STRESS FIELDS OF THE ORIGINAL AND PROPOSED DESIGNS USING FEM, RPIM AND NNRPIM FOR 2D MODEL. | 76 |
| TABLE 11 - DISPLACEMENT AND STRESS FIELDS OF THE ORIGINAL AND PROPOSED DESIGNS USING FEM, RPIM AND NNRPIM FOR 3D MODEL. | 77 |
| TABLE 12 – STRUCTURAL ANALYSIS RESULTS FOR 2D MODEL. | 78 |
| TABLE 13 – STRUCTURAL ANALYSIS RESULTS FOR 3D MODEL. | 78 |

INDEX

| | |
|---|-----|
| ABSTRACT | VII |
| 1 INTRODUCTION | 23 |
| 1.1 Framework | 23 |
| 1.2 Motivation..... | 23 |
| 1.3 Objectives..... | 23 |
| 1.4 Document Structure..... | 24 |
| 2 NUMERICAL METHODS..... | 27 |
| 2.1 FEM | 27 |
| 2.2 Meshless Methods | 27 |
| 2.2.1 Meshless Methods: State of the Art..... | 28 |
| 2.2.2 Numerical Integration | 29 |
| 2.2.2.1 RPIM..... | 29 |
| 2.2.2.2 NNRPIM | 31 |
| 2.2.3 Nodal Connectivity | 33 |
| 2.2.3.1 RPIM..... | 33 |
| 2.2.3.2 NNRPIM | 34 |
| 2.2.4 Interpolation Shape Functions | 36 |
| 2.3 Solid Mechanics Fundamentals..... | 39 |
| 3 STRUCTURAL OPTIMIZATION | 42 |
| 3.1 Structural Optimization: State of the art | 43 |
| 3.1.1 Recent works | 45 |
| 4 NUMERICAL EXAMPLES | 51 |
| 4.1 Numerical example 1: Cantilever Beam..... | 51 |

| | | |
|-------|---|----|
| 4.1.1 | Domain discretization type influence..... | 52 |
| 4.1.2 | Mesh influence and optimization parameters | 53 |
| 4.1.3 | Computational Time | 58 |
| 4.1.4 | Cantilever Beam Variant..... | 61 |
| 4.2 | Numerical Example 2: Simply supported Beam | 63 |
| 4.2.1 | Mesh influence and optimization parameters | 64 |
| 4.2.2 | Computational Time | 68 |
| 4.3 | Handbrake Lever | 70 |
| 4.3.1 | 2D | 73 |
| 4.3.2 | 3D | 74 |
| 4.3.3 | Proposed optimal topology design and structural analysis..... | 75 |
| 5 | CONCLUSIONS AND PROPOSALS OF FUTURE WORKS | 81 |
| 5.1 | Future Works..... | 82 |
| 6 | REFERENCES AND OTHER SOURCES OF INFORMATION | 85 |

INTRODUCTION

| | | |
|-----|-------------------------|----|
| 1 | INTRODUCTION | 23 |
| 1.1 | Framework | 23 |
| 1.2 | Motivation..... | 23 |
| 1.3 | Objectives..... | 23 |
| 1.4 | Document Structure..... | 24 |

1 INTRODUCTION

1.1 Framework

The search for better and more efficient parts to keep up to the competition inside the industry has always been a part of the objectives of a company. However, it gets to a point where no major improvements can be made to those parts. This is where structural optimization plays a big role, since performances can be optimized to its maximum and even reduce resources usage, and therefore production costs.

Over the last decades, mesh-based numerical methods such as Finite Element Method (FEM), have been used to analyse and optimize diverse structural components. However, the application of these methods in parts with complex geometries and large deformation problems result in lower accuracy and solution stability. Thus, in the last decades, numerical meshless methods have been growing in popularity among the communities since they can adjust better to complex geometries and still obtain precise results.

1.2 Motivation

Since more and more industries rely on structural optimization to improve the performance of their products, it is of great importance to keep exploring and investigating this area of study.

Nowadays, there is the civic duty and imposed objectives for companies to reduce their emissions and resource usage in order to move towards an efficient and sustainable world. Structural topology optimization allows to achieve these objectives because it removes a significant amount of material and therefore less resources are wasted, as well as emissions on the production of these parts.

Although meshless methods have been studied and applied in various research works in the last decades and proven to be a good option compared with the mesh-based methods, there are still few research works regarding this subject and room for improvement in some aspects. Hereupon, this thesis is an important contribution for the developed work that has been carried out around this area.

1.3 Objectives

The main focus of this thesis is to study the structural topology optimization using meshless methods and comparing its results with the mesh-based method FEM, to verify if the meshless methods are reliable and capable to produce accurate solutions.

Thus, the objectives of the present work can be summarized as it follows:

- Analysis of benchmark problems, to acquire autonomy in the use of the proposed software;
- Study domain discretization influence on optimized solutions;
- Study mesh and optimization parameters influence on optimized solutions;
- Compare the computational time between the methods used;
- Verification of the benefits of applying structural topology optimization into an industrial application;
- Demonstrate the potentialities of using meshless methods over mesh-based methods.

1.4 Document Structure

The present work is divided in five chapters, with them being divided into various sections.

Chapter 1, is a brief summary on the importance of this kind of work. It is also described the main objectives of this work.

In chapter 2, numerical methods are introduced. Firstly, mesh-based methods are introduced following the focus of this work: meshless methods. In this chapter is also provided a state of the art of the meshless methods, as well as formulations of the numerical methods used throughout the development of this work.

In chapter 3, it is explained the importance of structural optimization in the industry. It is provided the state of the art on this kind of research area, as well as recent and innovative works developed in the last two years.

Chapter 5, is dedicated to the usage of structural topology optimization into two benchmark examples and one industrial application, using mesh-based and meshless numerical methods.

The chapter 5 presents the conclusions obtained from this work, and future works.

BIBLIOGRAPHIC WORK

| | | |
|---------|---|----|
| 2 | NUMERICAL METHODS..... | 27 |
| 2.1 | FEM | 27 |
| 2.2 | Meshless Methods | 27 |
| 2.2.1 | Meshless Methods: State of the Art..... | 28 |
| 2.2.2 | Numerical Integration | 29 |
| 2.2.2.1 | RPIM..... | 29 |
| 2.2.2.2 | NNRPIM | 31 |
| 2.2.3 | Nodal Connectivity | 33 |
| 2.2.3.1 | RPIM..... | 33 |
| 2.2.3.2 | NNRPIM | 34 |
| 2.2.4 | Interpolation Shape Functions | 36 |
| 2.3 | Solid Mechanics Fundamentals..... | 39 |
| 3 | STRUCTURAL OPTIMIZATION | 42 |
| 3.1 | Structural Optimization: State of the art | 43 |
| 3.1.1 | Recent works | 45 |

2 Numerical Methods

Over the last decades, the use of numerical methods to solve partial differential equations has been an essential key to solve various problems of engineering. However, in the last two decades meshless methods have gained some attention over the mesh-based numerical methods like FEM and BEM, since these ones have some innate limitations when dealing with large deformations problems [1].

In this chapter, firstly, it is presented an overview of FEM and afterwards an explanation of the meshless method that will be used in this work.

2.1 FEM

FEM origins can be traced back to the 1950's, firstly by M. J. Turner at Boeing where he generalized and perfected the Direct Stiffness Method. During the 1950's and 1960's it started being popularized by four academics: J. H. Argyris, R. W. Clough, H. C. Martin and O. C. Zienkiewicz who were responsible to extend the method from aerospace industry into wider range of engineering applications [2].

Nowadays, FEM is one of the most used numerical methods in computation mechanics and can be used in diverse fields of applications such as the mechanical engineering [3].

FEM is a mesh-dependent approximation method where the continuum domain is discretized into a set of small finite elements, and each of these elements is connected to the others through common interfaces (nodes), forming a mesh. Shape functions are then constructed based in these elements in order to establish the system equations that can be used to determine the approximate solution in any point of interest of the domain [4].

The simple discretization concept, the low computational cost and the facility to program, makes FEM one compact numerical method when compared to the others. Nevertheless, when dealing with large deformation problems that require a constant update of the discretization mesh, FEM lacks on accuracy and solution stability, which brings disadvantages in some computational mechanics fields. Beyond that, in fluid flow analysis, the constant mesh update increases the computational cost [3].

2.2 Meshless Methods

In opposition to the mesh-based numerical methods, in meshless methods the nodes can be arbitrary distributed, once the field functions are approximated within an

influence-domain rather than an element. Contrary to FEM no-overlap rule between elements, influence-domains may and must overlap each other in meshless methods [4]. Further in this chapter, it is presented the formulation of two meshless methods, the RPIM and the NNRPIM.

2.2.1 Meshless Methods: State of the Art

Meshless methods were developed with the objective to eliminate the difficulties associated with reliance on a mesh to construct the approximation [5]. Meshless methods can be divided in two classes: approximation meshless methods and interpolation meshless methods. The first class to appear were the approximation meshless methods [3, 6].

One of the oldest meshless methods is the Smooth Particle Hydrodynamics (SPH), by Lucy and Gingold and Monaghan [5]. This method is based in the kernel approximation and it was born to solve problems in astrophysics and, later on, widely used to solve free surface flow problems [3, 5]. In the same period, the diffuse element method (DEM) appeared, which is considered by many as the first mature meshless method for solid mechanics. The DEM constructs the approximation shape functions using the moving least square (MLS) approximants. In 1994, Belytschko and co-workers improved the DEM and developed one of the most popular meshless method, the element-free Galerkin method (EFGM), as it was one of the first meshless methods based on a global weak form. One year later, the SPH was modified to suit the demands of solid mechanics problems originating the reproducing kernel particle method (RKPM). Another method that derived from SPH was the meshless local Petroc-Galerkin (MLPG), a very popular method based on local weak forms [3–6]. The main difference between MLPG method and others such as EFGM and RKPM is that the local weak forms are generated on overlapping subdomains rather than using global weak forms. The integration of the weak form is then carried out in these local subdomains. The notion “truly” meshless was introduced by Atluri, since this method does not require a construction of a background mesh for integration purposes [5]. Another approximation method, distinct from the previous, is the Radial Basis Function Method (RBFM). It uses the radial basis functions, respecting a Euclidean norm, to approximate the variable fields within the entire domain or in small domains.

Despite the fact that approximant meshless methods have been successfully applied in computational mechanics, all they lack the Kronecker delta property on the shape functions, which hinders the imposition of natural boundary conditions [4]. To solve this problem, interpolation meshless methods were developed in the last decades, such as the natural element method (NEM) and the point interpolation method (PIM). Later, an efficient version of PIM and one of the most applied in computational mechanics was developed, the Radial Point Interpolation Method (RPIM), which combines the polynomial basis of the PIM with a radial basis function. More recently, the combination between the NEM and the RPIM originated the Natural Neighbour Radial Point Interpolation Method (NNRPIM) [3, 4].

2.2.2 Numerical Integration

In order to perform the numerical integration of the integro-differential equations that rule the physical phenomenon, numerical methods using the Galerkin weak formulation require the construction of a background integration mesh and this is a significant percentage of the final computational cost of the analysis. The meshless methods used in this work use two different integration schemes, the Gauss-Legendre quadrature scheme and a nodal based integration scheme [3, 4].

2.2.2.1 RPIM

In the Gauss-Legendre integration, the solid domain is divided in a regular grid, as Fig. 1 indicates.

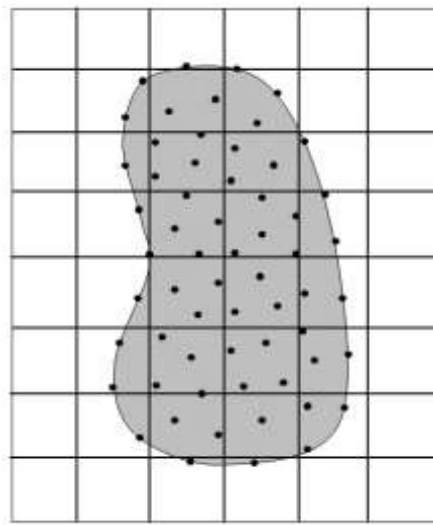


Fig. 1 - General Gaussian Integration mesh

Then each grid-cell, Fig. 2, is transformed in an isoparametric square and filled with integration points, respecting the Gauss-Legendre quadrature rule. In Fig. 2 the cell is filled with 2×2 integration point. After that, the Cartesian coordinates of the quadrature are obtained using isoparametric interpolation functions. The weight of each integration point can be acquired multiplying the isoparametric weight of the integration point with the Jacobian matrix determinant of the respective grid-cell, Fig. 3.

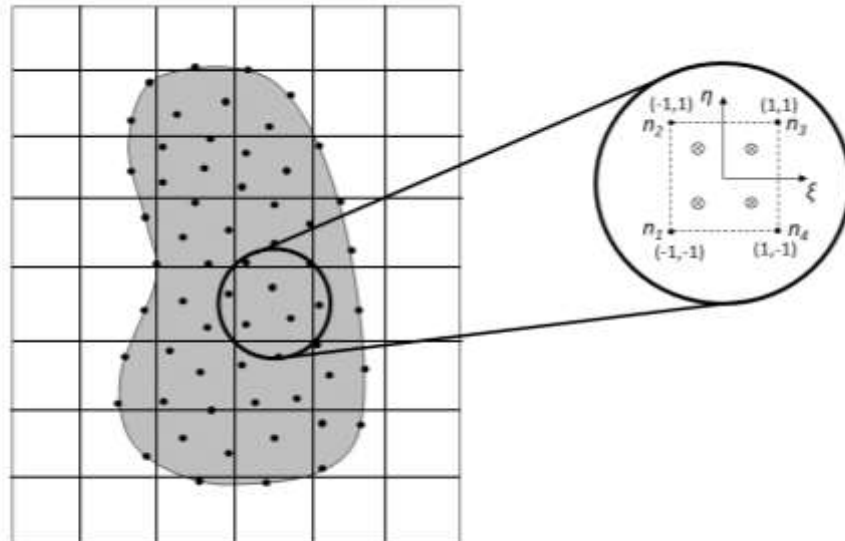


Fig. 2 - Transformation of the initial quadrilateral into an isoparametric square shape (2 x 2 integration points per integration cell)

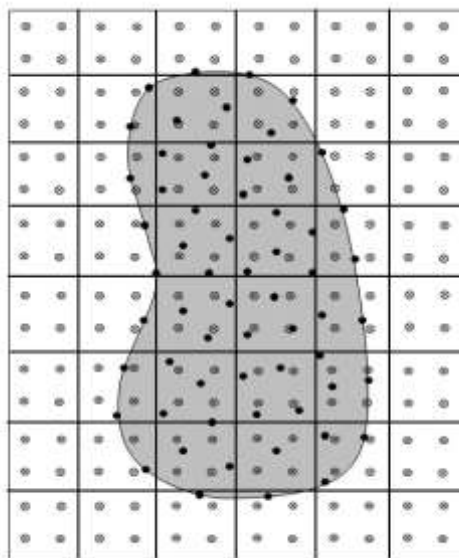


Fig. 3 - General Gaussian Integration mesh

Notice that, if the grid fits the solid domain no post-treatment is required. However, if the grid is larger than the solid domain all the integration points outside the solid domain must be removed, Fig. 4.

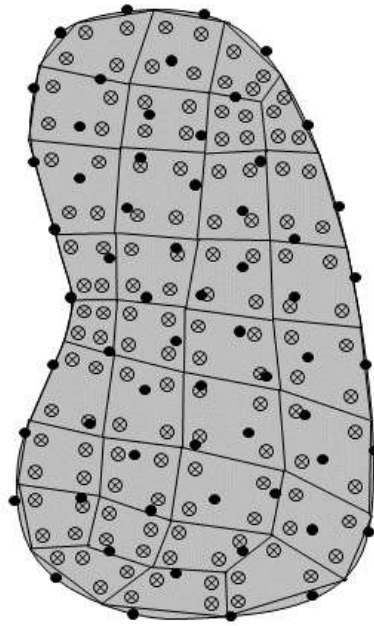


Fig. 4 - Fitted Gaussian mesh

Generally, in meshless methods, it is used regular quadrature integration meshes, since it presents lower computational costs and it is simpler to apply.

Consider the function $F(\mathbf{x})$ defined in the domain Ω to perform the numerical integration. The global integration can be expressed by,

$$\int_{\Omega} \mathbf{F}(\mathbf{x}) d\Omega = \sum_{i=1}^{n_g} \hat{w}_i \mathbf{F}(\mathbf{x}_i) \quad (1)$$

where \hat{w}_i is the weight of the integration point \mathbf{x}_i .

2.2.2.2 NNRPIM

The main difference between Nodal Based integration scheme and the Gauss-Legendre integration, is that the background integration scheme is constructed using uniquely the nodal distribution spatial information. Making meshless methods using this numerical integration scheme truly meshless, since no other information is necessary to: establish the nodal connectivity, determine the integration points and construct the shape functions [3, 4].

After the domain discretization with a nodal distribution, the Voronoï cells of each node are determined. The determination of Voronoï cells is presented in section 2.2.3.2. Depending on the nodal discretization being irregular or regular, the areas that will be established by the Voronoï cells can be quadrilaterals or triangles, respectively. If the domain $\Omega \subset \mathbb{R}^2$ is discretized by an irregular nodal set $\mathbf{N} = \{n_1, n_2, \dots, n_6\}$, Fig. 5, this allows to construct the Voronoï cell V_I of node n_I and to determine the corners P_{Ii} of the polygonal shape defined by V_I , Fig. 5 (a). After that, the middle points, M_{Ii} ,

between n_I and each neighbour nodes are obtained, Fig. 5 (b). As a result, the Voronoi cells are divided in n quadrilateral sub-cells, S_{Ii} , being n the number of natural neighbours of node n_I , Fig. 5 (c).

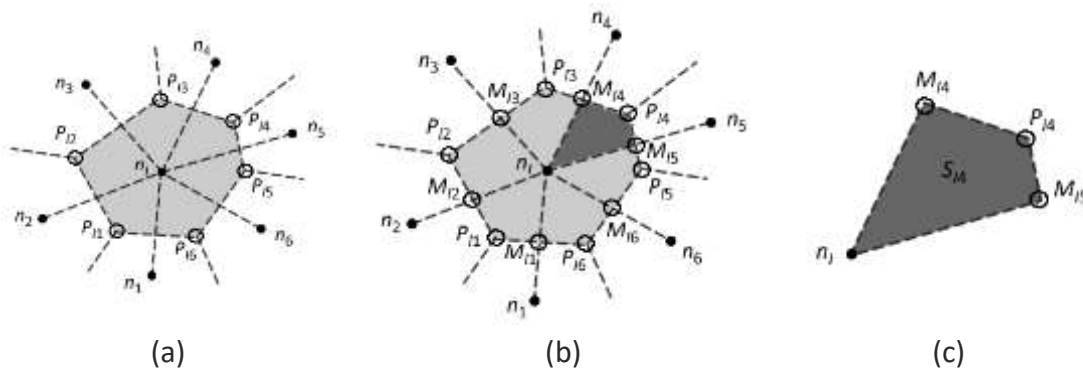


Fig. 5 – a) Voronoi cell and the intersection points (P_{ii}); b) Middle points (M_{ii}) and the generated quadrilaterals; c) Quadrilateral $\overline{n_1 M_{14} P_{14} M_{15}}$

However, if the domain $\Omega \subset \mathbb{R}^2$ is discretized by a regular nodal set $N = \{n_1, n_2, \dots, n_6\}$, Fig. 6 (a), this will result in a Voronoi cell divided in n triangular sub-cells, S_{Ii} , being n the number of natural neighbours of node n_I , Fig. 6 (c).

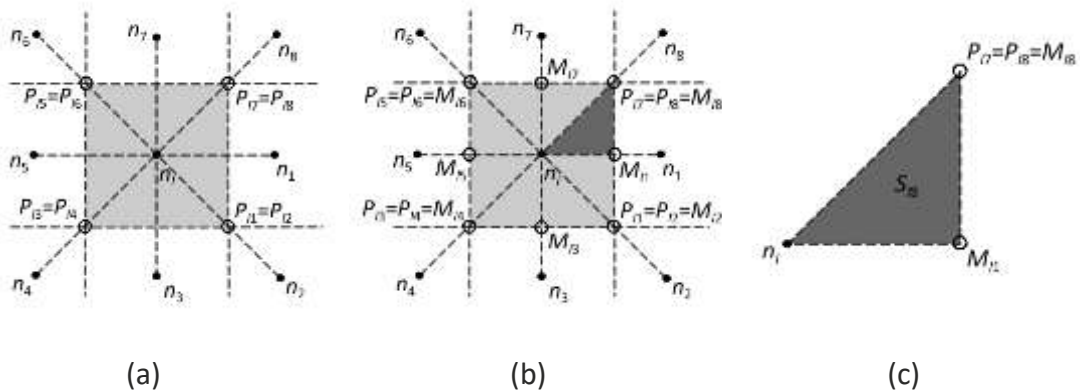


Fig. 6 - a) Voronoi cell and the intersection points (P_{ii}); b) Middle points (M_{ii}) and the generated triangles; c) Triangle $\overline{n_1 P_{17} M_{18}}$

Afterwards, it is used the Gauss-Legendre numerical integration in order to establish the numerical integration. Thus, the sub-cell is subdivided again, however in this case only as quadrilaterals. Firstly, it is determined the centre of the geometric shape, x_C , then middles points on the quadrilateral edges are determined, x_{ij} , and as a result new sub-quadrilaterals are defined, Fig. 7. Then, by applying the Gauss-Legendre quadrature to the obtained sub-quadrilaterals, it is possible to obtain the integration points, Fig. 7. This process permits to fill each sub-quadrilateral with $k \times k$ integration points.

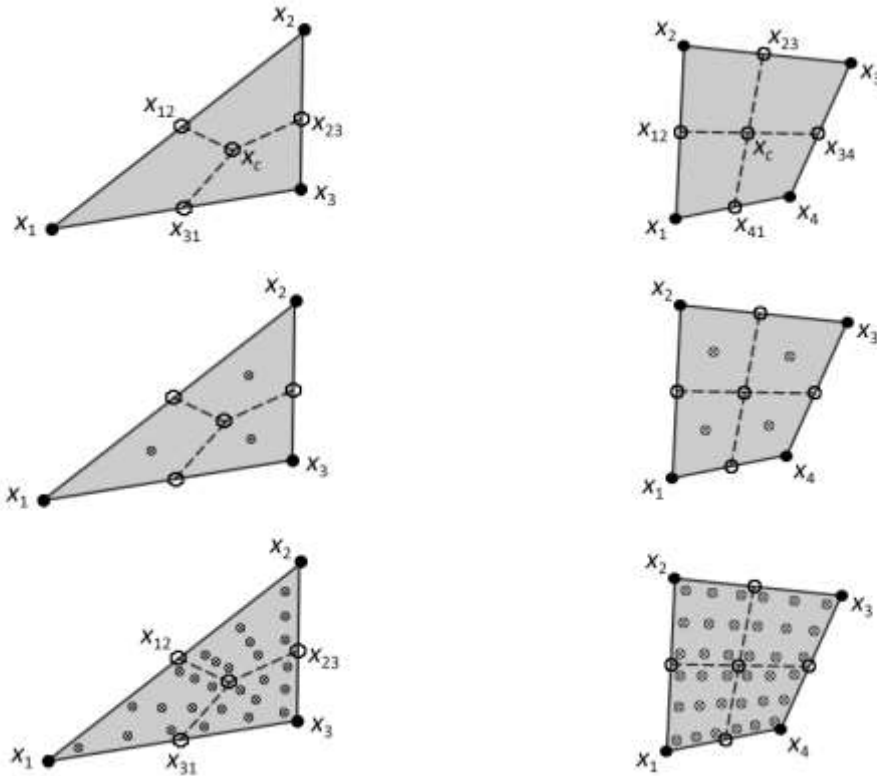


Fig. 7 – Triangular and quadrilateral shapes and their respective integration points x_i using the Gauss-Legendre integration scheme

The integration weight of each integration point x_i is obtained using the expression,

$$\hat{w}_I = w_\eta w_\xi \left(\frac{A^\square}{4} \right) \quad (2)$$

being A^\square the area of the respective sub-quadrilateral, and w_η and w_ξ are the Gauss-Legendre quadrature weights for an isoparametric quadrilateral cell.

2.2.3 Nodal Connectivity

2.2.3.1 RPIM

In meshless methods, since there is no nodal interdependency, the nodal connectivity is imposed after the discretization of the domain. In RPIM the nodal connectivity is obtained by the overlap of the influence-domain of each node. These influence-domains are found by searching nodes inside an area or volume, respectively for the 2D problem and for the 3D problem, concentric with an interest (integration) point. However, the size or shape variation of these influence-domains can affect the performance and the final solution of the meshless method, Fig. 8 (a).

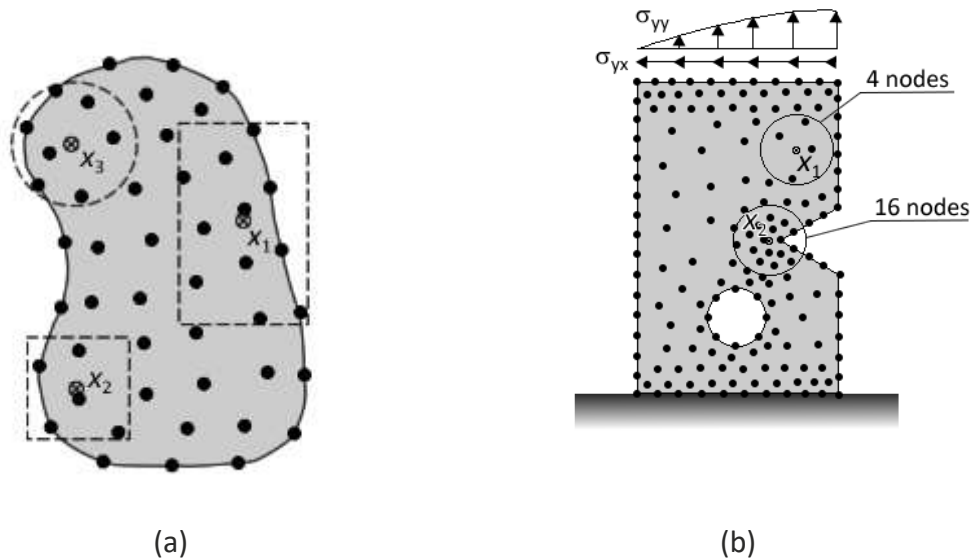


Fig. 8 – a) Influence-domains with different sizes and shapes; b) Example of a bad choice in the size of the influence-domain

Therefore, it is important that all the influence-domains in the problem contain approximately the same number of nodes, otherwise this can lead to unbalanced influence-domains, Fig. 8 (b), implying loss of accuracy. To avoid that, RPI uses variable influence-domains, centred in the interest point x_i , which will perform a radial search to encompass n nodes.

2.2.3.2 NNRPIM

In the NNRPIM, the way to determine the nodal connectivity is by using mathematical concepts such as the Voronoï diagram. These influence-domains are based on the geometric and spatial relations between the Voronoï cells obtained from the Voronoï diagram, therefore, the influence-domains are called influence-cells. The Voronoï diagram uses the concept of the natural neighbours and is applied to the nodal distribution in order to create the influence-cells.

Consider the problem domain $\Omega \subset \mathbb{R}^2$ discretized by a nodal set $N = \{n_1, n_2, \dots, n_N\} \in \mathbb{R}^2$ with $X = \{x_1, x_2, \dots, x_N\}$ coordinates. The Voronoï diagram of N corresponds to the division of the domain in Voronoï cells, V_i , which can be closed or convex. Each Voronoï cell is associated to the node n_i in a way that any point in the interior of V_i is closer to this node than any other node $n_j \in N \wedge i \neq j$. The Voronoï cell is expressed by,

$$V_i = \{x_l \in \Omega \subset \mathbb{R}^d : \|x_l - x_i\| < \|x_l - x_j\|, \quad \forall i \neq j\} \quad (3)$$

being x_i an interest point and $\|\cdot\|$ the Euclidian metric norm. In the Fig. 9 it is represented the generic way to obtain a 2D Voronoï diagram.

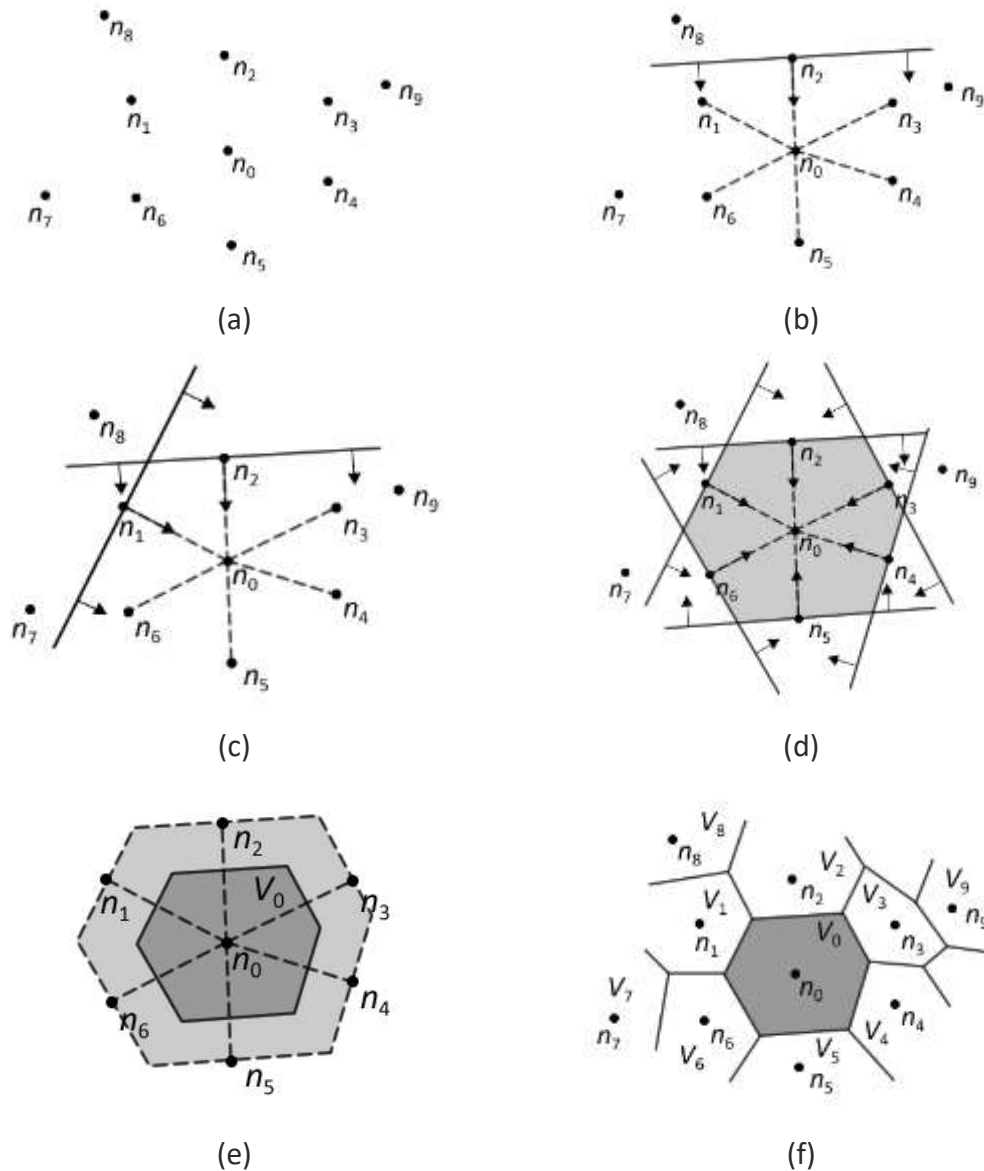


Fig. 9 – a) Initial nodal set of potential neighbour nodes of node n_0 ; b) First trial plane; c) Second trial plane; d) Final trial cell containing just the natural neighbours of node n_0 ; e) Node n_0 and the respective Voronoi cell V_0 ; f) Voronoi diagram

Considering the nodal set from Fig. 9, in order to determine the Voronoi cell V_0 of node n_0 , nodes n_1 to n_6 are chosen as potential neighbours of node n_0 . After that, one of these nodes is selected, in this case the node n_2 . Thus, the vector \mathbf{u}_{20} is determined,

$$\mathbf{u}_{20} = \frac{(\mathbf{x}_0 - \mathbf{x}_2)}{\|\mathbf{x}_0 - \mathbf{x}_2\|} \quad (4)$$

being $\mathbf{u}_{20} = \{u_{20}, v_{20}, w_{20}\}$. With this, it is possible to determine the plane π_{20} ,

$$u_{20}x + v_{20}y + w_{20}z = (u_{20}x_2 + v_{20}y_2 + w_{20}z_2) \quad (5)$$

Afterwards, all the nodes that do not satisfy the following inequation,

$$u_{20}x + v_{20}y + w_{20}z \geq (u_{20}x_2 + v_{20}y_2 + w_{20}z_2) \quad (6)$$

are excluded as natural neighbours of the node n_0 , Fig. 9 (b). This process is repeated for all the domain nodes, Fig. 9 (d). In the end, only the neighbour nodes of node n_0 will remain, Fig. 9 (e).

Repeating the process to determine a Voronoï cell for each node discretizing the domain, it is possible to construct the Voronoï diagram, Fig. 9 (f). In the Voronoï diagram, two types of influence-cells can be established, Fig. 10, according to the level of nodal connectivity: the first-degree influence cells (a) and the second-degree influence cells (b).

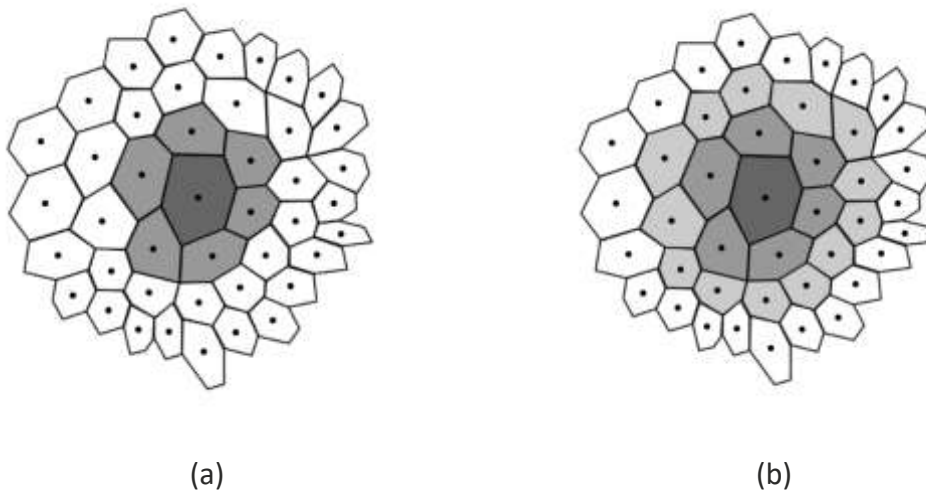


Fig. 10 – a) First degree influence-cell; b) Second degree influence-cell

When considering a first-degree influence cell only the natural neighbours of the point of interest are taken into consideration. However, if a second degree influence cell is considered, not only the natural neighbours of the point of interest are taken into consideration, but also the natural neighbours of these first ones, Fig. 10 (b). Being that the second-degree influence cell is larger than the first-degree, the second-degree influence cell, generally, offers better results.

2.2.4 Interpolation Shape Functions

In order to obtain a numerical solution, firstly we need to interpolate the unknown field functions. Both RPIM and NNRPIM, use the Radial Point Interpolators (RPI) technique to construct the respective interpolation shape functions. RPI combines polynomial basis functions $p(x)$ with radial basis functions $r(x)$ [3]. Besides that, since RPI possesses the Kronecker delta property, it permits a simpler imposition of the essential boundary conditions.

Considering the function $u(x)$, defined in the domain Ω , and discretized by a set of n nodes, at an interest point x_i , the function $u(x)$ contains all the interest points of the influence domain and can be expressed as,

$$\begin{aligned}
 u(\mathbf{x}_I) &= \sum_{i=1}^n r_i(\mathbf{x}_I) a_i(\mathbf{x}_I) + \sum_{j=1}^m p_j(\mathbf{x}_I) b_j(\mathbf{x}_I) \\
 &= \mathbf{r}^T(\mathbf{x}_I) \mathbf{a}(\mathbf{x}_I) + \mathbf{p}^T(\mathbf{x}_I) \mathbf{b}(\mathbf{x}_I)
 \end{aligned} \tag{7}$$

which can be written as,

$$u(\mathbf{x}_I) = \{\mathbf{r}(\mathbf{x}_I)^T, \mathbf{p}(\mathbf{x}_I)^T\} \begin{Bmatrix} \mathbf{a}(\mathbf{x}_I) \\ \mathbf{b}(\mathbf{x}_I) \end{Bmatrix} \tag{8}$$

being $a_i(\mathbf{x}_I)$ and $b_i(\mathbf{x}_I)$ the non-constant coefficients of $\mathbf{r}(\mathbf{x}_I)$ and $\mathbf{p}(\mathbf{x}_I)$ respectively, which can be written as,

$$\mathbf{r}(\mathbf{x}_I) = \{r_1(\mathbf{x}_I), r_2(\mathbf{x}_I), \dots, r_n(\mathbf{x}_I)\}^T \tag{9}$$

$$\mathbf{p}(\mathbf{x}_I) = \{p_1(\mathbf{x}_I), p_2(\mathbf{x}_I), \dots, p_m(\mathbf{x}_I)\}^T \tag{10}$$

$$\mathbf{a}(\mathbf{x}_I) = \{a_1(\mathbf{x}_I), a_2(\mathbf{x}_I), \dots, a_n(\mathbf{x}_I)\}^T \tag{11}$$

$$\mathbf{b}(\mathbf{x}_I) = \{b_1(\mathbf{x}_I), b_2(\mathbf{x}_I), \dots, b_m(\mathbf{x}_I)\}^T \tag{12}$$

This method uses the multi-quadrics radial basis function (MQ-RBF) [3, 7], which is defined by,

$$r(\mathbf{x}_I) = (d_{ii}^2 + c^2)^p \tag{13}$$

being c and p two MQ-RBF shape parameters defined in the literature as $c = 0.0001$ and $p = 1.0001$, respectively, in order to obtain accurate results, and d_{ii} the Euclidian norm between the integration point \mathbf{x}_I and the neighbour node \mathbf{x}_i ,

$$d_{ii} = \sqrt{(\mathbf{x}_i - \mathbf{x}_I)^2 + (\mathbf{y}_i - \mathbf{y}_I)^2} \tag{14}$$

The RPI formulation requires a polynomial basis function, which for 2D problems can be defined as,

$$\mathbf{p}(\mathbf{x})^T = [1, x, y, x^2, xy, y^2, \dots] \tag{15}$$

To assure a single solution, the polynomial equation needs to be included in the system of equations,

$$\sum_{i=1}^n p_j(\mathbf{x}_i) a_i(\mathbf{x}_i) = 0 \tag{16}$$

considering equation (8), and the previous assumptions, the function can be reformulated to,

$$\begin{Bmatrix} \mathbf{u}_s \\ \mathbf{0} \end{Bmatrix} = \begin{bmatrix} \mathbf{R} & \mathbf{P} \\ \mathbf{P}^T & \mathbf{0} \end{bmatrix} \begin{Bmatrix} \mathbf{a} \\ \mathbf{b} \end{Bmatrix} = \mathbf{M} \begin{Bmatrix} \mathbf{a} \\ \mathbf{b} \end{Bmatrix} \quad (17)$$

where \mathbf{u}_s , \mathbf{R} and \mathbf{P} , considering a 2D problem, can be defined as,

$$\mathbf{u}_s = \{u_1, u_2, \dots, u_n\}^T \quad (18)$$

$$\mathbf{R} = \begin{bmatrix} R(r_{11}) & R(r_{21}) & \dots & R(r_{n1}) \\ R(r_{12}) & R(r_{22}) & \dots & R(r_{n2}) \\ \vdots & \vdots & \ddots & \vdots \\ R(r_{1n}) & R(r_{2n}) & \dots & R(r_{nn}) \end{bmatrix} \quad (19)$$

$$\mathbf{P} = \begin{bmatrix} 1 & x_1 & y_1 \\ 1 & x_2 & y_2 \\ \vdots & \vdots & \vdots \\ 1 & x_n & y_n \end{bmatrix} \quad (20)$$

Solving the following equation,

$$\begin{Bmatrix} \mathbf{a} \\ \mathbf{b} \end{Bmatrix} = \mathbf{M}^{-1} \begin{Bmatrix} \mathbf{u}_s \\ \mathbf{0} \end{Bmatrix} \quad (21)$$

$$\mathbf{M}^{-1} = \begin{bmatrix} \mathbf{R} & \mathbf{P} \\ \mathbf{P}^T & \mathbf{0} \end{bmatrix}^{-1} \quad (22)$$

the equation (17) can be solved to determine the non-constant coefficients \mathbf{a} and \mathbf{b} . Replacing in the equation (8), the shape functions can be expressed as,

$$u(\mathbf{x}_I) = \{\mathbf{r}(\mathbf{x}_I)^T, \mathbf{p}(\mathbf{x}_I)^T\} \mathbf{M}^{-1} \begin{Bmatrix} \mathbf{u}_s \\ \mathbf{0} \end{Bmatrix} = \{\Phi(\mathbf{x}_I), \Psi(\mathbf{x}_I)\} \begin{Bmatrix} \mathbf{u}_s \\ \mathbf{0} \end{Bmatrix} \quad (23)$$

Where $\Phi(\mathbf{x}_I)$ is the shape function vector and $\Psi(\mathbf{x}_I)$ is a vector with no relevant physical meaning,

$$\Psi(\mathbf{x}_I) = \{\psi_1(\mathbf{x}_I), \psi_2(\mathbf{x}_I), \dots, \psi_m(\mathbf{x}_I)\} \quad (24)$$

Since this method possesses the Kronecker delta property δ_{ij} ,

$$\varphi_i(\mathbf{x}_j) = \delta_{ij} \quad (25)$$

for which,

$$\delta_{ij} = \begin{cases} 1, & i = j \\ 0, & i \neq j \end{cases} \quad (26)$$

allowing to impose directly the essential boundary conditions in the stiffness matrix. Thus, the RPI shape function, $\Phi(\mathbf{x}_I)$, can be defined as,

$$\Phi(\mathbf{x}_I) = \{\varphi_1(\mathbf{x}_I), \varphi_2(\mathbf{x}_I), \dots, \varphi_n(\mathbf{x}_I)\} \quad (27)$$

obtaining,

$$\begin{aligned} \{\Phi(\mathbf{x}_I), \Psi(\mathbf{x}_I)\} &= \{\mathbf{r}(\mathbf{x}_I)^T \mathbf{p}(\mathbf{x}_I)^T\} \mathbf{M}^{-1} \\ &= \{\varphi_1(\mathbf{x}_I), \varphi_2(\mathbf{x}_I), \dots, \varphi_n(\mathbf{x}_I), \psi_1(\mathbf{x}_I), \dots, \psi_m(\mathbf{x}_I)\} \end{aligned} \quad (28)$$

being n the number of nodes inside the influence domain, and m the number of polynomial terms of the polynomial basis function, where the $n \gg m$ rule should be respected in order to assure a stable function [4].

2.3 Solid Mechanics Fundamentals

If loads are applied to solids or structures these become stressed. Those stresses lead to strains, which are deformation ratios. Solid Mechanics and Structural Mechanics deals with the relationship between stress and strain and the relationship between strain and displacements, for a given solid with defined boundary conditions.

Depending on the material strain-stress curve, solids can have different behaviours. Solids can be elastic where the deformation in the solid caused by loading fully disappears with the unloading, or they can be plastic where they can show a residual deformation (which cannot be naturally recovered) that remains even after the unload.

Material properties can also be divided in two types. Materials that have the same properties in all directions, which are called isotropic materials. For this type of material, it is only necessary to determine two independent material constants: the Young's modulus and the Poisson's ratio. On the other hand, if the material has different properties in different directions, they are called anisotropic, and for these ones several material constants are needed depending on the degree of anisotropy.

Also, boundary conditions, which can be applied through forces or displacements, must be taken into consideration, as they play an important paper in mechanics. In this work only static forces will be considered, meaning that the stress, strain and displacement will not be considered as a function of time [4].

Throughout this section, the fundamentals of Solid Mechanics will be presented. Considering $\Omega \subset \mathbb{R}^2$, the solid domain contained in Γ , where $\Gamma \in \Omega : \Gamma_u \cup \Gamma_t = \Gamma \wedge \Gamma_u \cap \Gamma_t \neq \emptyset$, where Γ_u is the essential boundary and Γ_t is the natural boundary, the linear elastostatic problem equilibrium equations can be expressed by,

$$\nabla \Lambda + \mathbf{b} = \mathbf{0} \text{ in } \Omega \quad (29)$$

where ∇ is the divergence operator, Λ is the Cauchy stress tensor, and \mathbf{b} is the body forces per unit volume. The natural boundary conditions are given by,

$$\Lambda \mathbf{n} = \bar{\mathbf{t}} \quad (30)$$

with $\bar{\mathbf{t}}$ being the traction on the natural boundary Γ_t and \mathbf{n} the unit outward normal to the boundary of domain Ω . The essential boundary conditions are imposed with,

$$\mathbf{u} = \bar{\mathbf{u}} \quad (31)$$

where $\bar{\mathbf{u}}$ is the prescribed displacement on the essential boundary Γ_u . The Galerkin weak form of equation (29) can be written as:

$$\int_{\Omega} \delta \boldsymbol{\varepsilon}^T \boldsymbol{\sigma} d\Omega - \int_{\Omega} \delta \mathbf{u}^T \mathbf{b} d\Omega - \int_{\Gamma_t} \delta \mathbf{u}^T \mathbf{t} d\Gamma = 0. \quad (32)$$

In NNRPIM, the discrete system of equations is firstly developed for every integration point [7]. After that, the local systems of equations are assembled into the global system of equations, and finally, the final equation system is solved. Using the interpolation functions $\varphi_i(\mathbf{x}_I)$ obtained from equation (28), it is possible to define for an interest point $\mathbf{x}_I \in \Omega$ the following approximation,

$$u(\mathbf{x}_I) = \sum_{i=1}^n \varphi_i(\mathbf{x}_I) u(\mathbf{x}_i) \quad (33)$$

being $u(\mathbf{x}_i)$ the nodal parameter of the i^{th} node belonging to the nodal set defining the influence-cell of interest node \mathbf{x}_I . Taking into consideration the previous equation, it is possible to obtain the virtual displacement approximation,

$$\begin{aligned} \delta u^h(\mathbf{x}_I) &= \begin{Bmatrix} \delta u^h(\mathbf{x}_I) \\ \delta v^h(\mathbf{x}_I) \end{Bmatrix} = \sum_{i=1}^n \begin{bmatrix} \varphi_i(\mathbf{x}_I) & 0 \\ 0 & \varphi_i(\mathbf{x}_I) \end{bmatrix} \begin{Bmatrix} \delta u^h(\mathbf{x}_i) \\ \delta v^h(\mathbf{x}_i) \end{Bmatrix} \\ &= \sum_{i=1}^n \mathbf{H}_i(\mathbf{x}_I) \delta \mathbf{u}(\mathbf{x}_i) \end{aligned} \quad (34)$$

and using the Hooke law, the strain and stress vectors on equation (32) can be correlated,

$$\boldsymbol{\varepsilon} = \mathbf{s} \boldsymbol{\sigma} \Leftrightarrow \begin{Bmatrix} \varepsilon_{xx} \\ \varepsilon_{yy} \\ \gamma_{xy} \end{Bmatrix} = \begin{bmatrix} S_{11} & S_{12} & S_{13} \\ S_{21} & S_{22} & S_{23} \\ S_{31} & S_{31} & S_{33} \end{bmatrix} \begin{Bmatrix} \sigma_{xx} \\ \sigma_{yy} \\ \tau_{xy} \end{Bmatrix} \quad (35)$$

where \mathbf{s} is the compliance elasticity matrix for the general anisotropic material case. For the pane stress and plane strain formulations, respectively, these can be defined as,

$$\mathbf{s}_{plane\ stress} = \begin{bmatrix} \frac{1}{E_{11}} & -\frac{\nu_{21}}{E_{22}} & 0 \\ -\frac{\nu_{12}}{E_{11}} & \frac{1}{E_{22}} & 0 \\ 0 & 0 & \frac{1}{G_{12}} \end{bmatrix} \quad (36)$$

$$\mathbf{s}_{plane\ strain} = \begin{bmatrix} \frac{1 - \nu_{31}\nu_{13}}{E_{11}} & -\frac{\nu_{12} + \nu_{31}\nu_{23}}{E_{22}} & 0 \\ -\frac{\nu_{12} + \nu_{32}\nu_{13}}{E_{11}} & \frac{1 - \nu_{32}\nu_{23}}{E_{22}} & 0 \\ 0 & 0 & \frac{1}{G_{12}} \end{bmatrix} \quad (37)$$

being E_{ij} the elasticity modulus, ν_{ij} the material Poisson coefficient, and G_{ij} the distortion modulus in material direction i and j . The stress vector can be obtained using the expression $\boldsymbol{\sigma} = \mathbf{c}\boldsymbol{\varepsilon}$, being $\mathbf{c} = \mathbf{s}^{-1}$. The virtual strain vector can be obtained using the following equation,

$$\delta\boldsymbol{\varepsilon} = \mathbf{L}\delta\mathbf{u} \Leftrightarrow \begin{Bmatrix} \delta\varepsilon_{xx} \\ \delta\varepsilon_{yy} \\ \delta\gamma_{xy} \end{Bmatrix} = \begin{bmatrix} \frac{\partial}{\partial x} & 0 \\ 0 & \frac{\partial}{\partial y} \\ \frac{\partial}{\partial y} & \frac{\partial}{\partial x} \end{bmatrix} \begin{Bmatrix} \delta u \\ \delta v \end{Bmatrix} \quad (38)$$

Using the equation (34) it is now possible to develop the virtual strain vector to the following expression:

$$\begin{aligned} \delta\boldsymbol{\varepsilon}(\mathbf{x}_I) &= \mathbf{L}\delta\mathbf{u}^h(\mathbf{x}_I) = \mathbf{L} \sum_{i=1}^n \mathbf{H}_i(\mathbf{x}_I)\delta\mathbf{u}(\mathbf{x}_i) = \sum_{i=1}^n [\mathbf{L}\mathbf{H}_i(\mathbf{x}_I)]\delta\mathbf{u}(\mathbf{x}_i) \\ &= \sum_{i=1}^n \mathbf{B}_i(\mathbf{x}_I)\delta\mathbf{u}(\mathbf{x}_i) \\ &= \sum_{i=1}^n \begin{bmatrix} \frac{\partial\varphi_i(\mathbf{x}_I)}{\partial x} & 0 \\ 0 & \frac{\partial\varphi_i(\mathbf{x}_I)}{\partial y} \\ \frac{\partial\varphi_i(\mathbf{x}_I)}{\partial y} & \frac{\partial\varphi_i(\mathbf{x}_I)}{\partial x} \end{bmatrix} \begin{Bmatrix} \delta u(\mathbf{x}_i) \\ \delta v(\mathbf{x}_i) \end{Bmatrix} \end{aligned} \quad (39)$$

Substituting the virtual strain vector $\delta\boldsymbol{\varepsilon}(\mathbf{x}_I)$ obtained in equation (39), the stress vector $\boldsymbol{\sigma}(\mathbf{x}_I) = \mathbf{c}\boldsymbol{\varepsilon}(\mathbf{x}_I) = \mathbf{c}\mathbf{L}\mathbf{u}(\mathbf{x}_I)$, and the virtual displacement vector $\delta\mathbf{u}^h(\mathbf{x}_I)$ from equation (34), the equation (32) can be rewrite for an interest point \mathbf{x}_I :

$$\begin{aligned} & \sum_{i=1}^n \sum_{j=1}^n \delta\mathbf{u}_i^T \int_{\Omega} \mathbf{B}_i^T \mathbf{c} \mathbf{B}_j d\Omega \mathbf{u}_j \\ & - \sum_{i=1}^n \delta\mathbf{u}_i^T \int_{\Omega} \mathbf{H}_i^T \begin{Bmatrix} b_x \\ b_y \end{Bmatrix} d\Omega - \sum_{i=1}^n \delta\mathbf{u}_i^T \int_{\Gamma_t} \mathbf{H}_i^T \begin{Bmatrix} t_x \\ t_y \end{Bmatrix} d\Gamma_t \\ & = 0 \end{aligned} \quad (40)$$

Finally, after assembling the stiffness matrices \mathbf{K}_I obtained for each interest point, the previous equation can be written as:

$$\delta\mathbf{u}^T [\mathbf{K}\mathbf{u} - \mathbf{f}_b - \mathbf{f}_t] = 0 \Leftrightarrow \mathbf{K}\mathbf{u} = \mathbf{f}_b + \mathbf{f}_t \quad (41)$$

3 Structural Optimization

Structural optimization is a specific field of computational mechanics that seeks to achieve the best performance for a structure, while satisfying various constraints such as a given amount of material or structural resistance or rigidity. Having an optimal structural design is becoming more and more important, since there is limited material resources, environmental impact and technological competition.

Over the last three decades the topic of structural optimization has been applied to a wide range of design problems in many industries, such as mechanical, automotive, and civil industries, achieving a state where a growing number of engineers and architects start to use it and benefit from the optimization techniques. The usage of structural optimization on these industries can be a possible way to reduce the weight of a structure and by that, reducing the cost of the production but still not neglecting the high-performance.

Structural optimization can be classified into three categories: size, shape and topology optimization. Size optimization is the easiest and earliest approach to improve structural performance, and its goal is to find the optimal design by changing the size variables such as the cross-sectional dimensions of trusses and frames, or the thicknesses of plates. Shape optimization modifies the predetermined boundaries to achieve the optimal designs, and it is mainly performed on continuum structures. Topology optimization for discrete structures, such as trusses and frames, can be

defined as the search for the optimal spatial order and connectivity of the bars. On the other hand, for continuum structures its goal is to find the optimal designs by determining the best locations and geometries of cavities in the design domains.

3.1 Structural Optimization: State of the art

Since the pioneer work of Michell [8] and the seminal work of Bendsøe and Kikuchi [9], structural topology optimization has become an effective design tool for obtaining efficient and lighter structures [10].

Continuum structural topology optimization has received extensive attention and progress over the past few years. Up to now, various families of structural topology optimization methods have been developed [10]. The structural topology optimization algorithms can be classified in various families: h-methods, e-methods and h/e-methods [11]. One of the most established families of methods is the one based on the homogenization approach first proposed by Bendsøe and Kikuchi [9], in which the structural form is represented by microstructures with voids and the material throughout the structure is redistributed by using an optimality criteria procedure. Another approach within this family is the power-law approach, which is also called the solid isotropic microstructure with penalization method (SIMP) and originally introduced by Bendsøe, has got a fairly general acceptance because of its computational efficiency and conceptual simplicity [9, 10]. Another well-known family of structural topology methods is the one based on the evolutionary structural optimization (ESO) approach proposed by Xie and Steven [12] in which the material in design domain inefficiently used can be slowly removed. An opposite evolutionary process called additive ESO (AESO) was then presented by Querin [13], where the structure evolves from a base which is the minimum structural form required to carry the load regardless of the stress levels. The material is then added to high stress region to improve its effect. It is found that the AESO can efficiently add material where it is most needed, however it does not require the capability to remove any material. Since there are situations where stressed elements should be removed from structures, it is advantageous to combine the additive attribute of AESO with the removing attribute of ESO. For this reason, a new methodology has emerged called bi-directional evolutionary structural optimization (BESO) proposed by Querin [14], which had the capability to add and remove material. Another e-methods were developed like the hard-kill method by Hinton and Sienz [15] and the soft-kill method by Mattheck [16]. The h/e-methods are hybrid methods which contain attributes of both h- and e-methods in differing degrees. The first of these methods was introduced by Fuchs [17], who characterized the topology material in a manner similar to that of the original microcell model of Bendsøe and Kikuchi, using the “Aboudi-cell” method.

With the growth of meshless methods, new studies of structural optimization started to be developed, and with them advantages over the studies using mesh-dependent methods. In a study carried by Juan [18], where he combined the EFGM with

the ESO to carry out the topology optimization of continuum structures, EFGM proved to be a good method to reduce the weight of structures by its simplicity and fast convergence when compared with the utilization of FEM, Fig. 11Fig. 14.

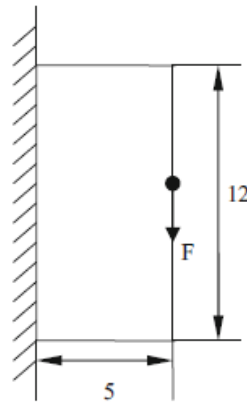


Fig. 11 - Cantilever beam model [18].

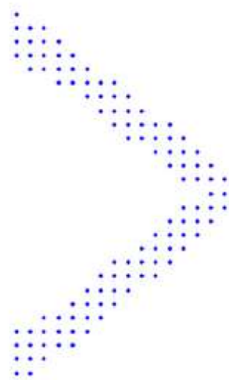


Fig. 12 - Optimization result obtained using EFGM [18].

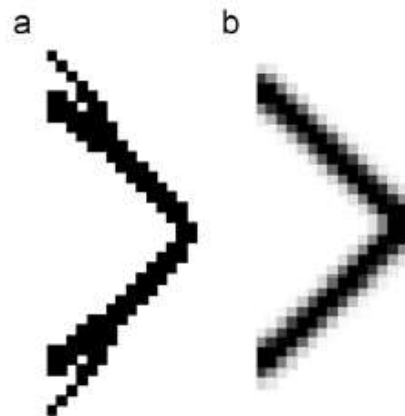


Fig. 13 - Optimization result using FEM without sensitivity filtering (a) and using sensitivity filtering (b) [18].

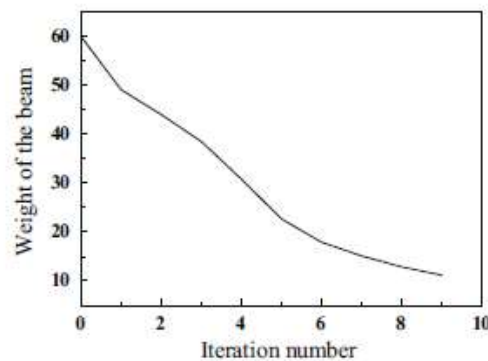


Fig. 14 - Convergence history of the cantilever beam using EFGM [18].

3.1.1 Recent works

The structural optimization has been under development over the last decade and last years, due to its important applications in many fields. In this chapter some of the recent works are exposed, as well as its achievements.

In a recent work proposed by Zhao [19], a new approach based on the graph theory and the set theory [20–22] is developed to control the number and size of interior holes of the optimized structures, because the structural complexity is usually characterized by the distribution and geometries of these holes. The study reveals that, by changing the initial layout of material, Fig. 15, or the constraints on the number, Fig. 16, and size of the interior holes, Fig. 17, it is possible to achieve distinct high performance structural designs. Therefore, the methodology presented holds great promise in the emerging field of human-computer interactive design.

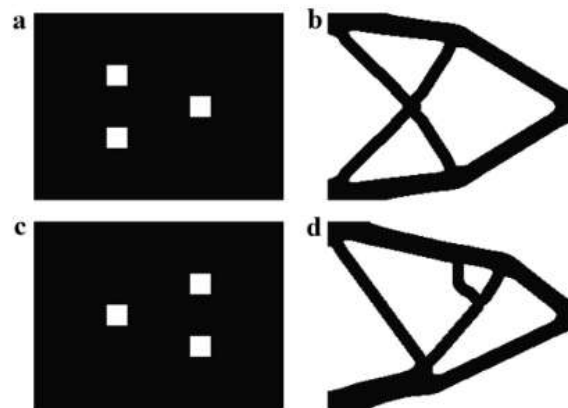


Fig. 15 - Influence of the initial material layout ((a) and (c)) on the optimized design of a cantilever beam ((b) and (d)) with structural complexity control [19].

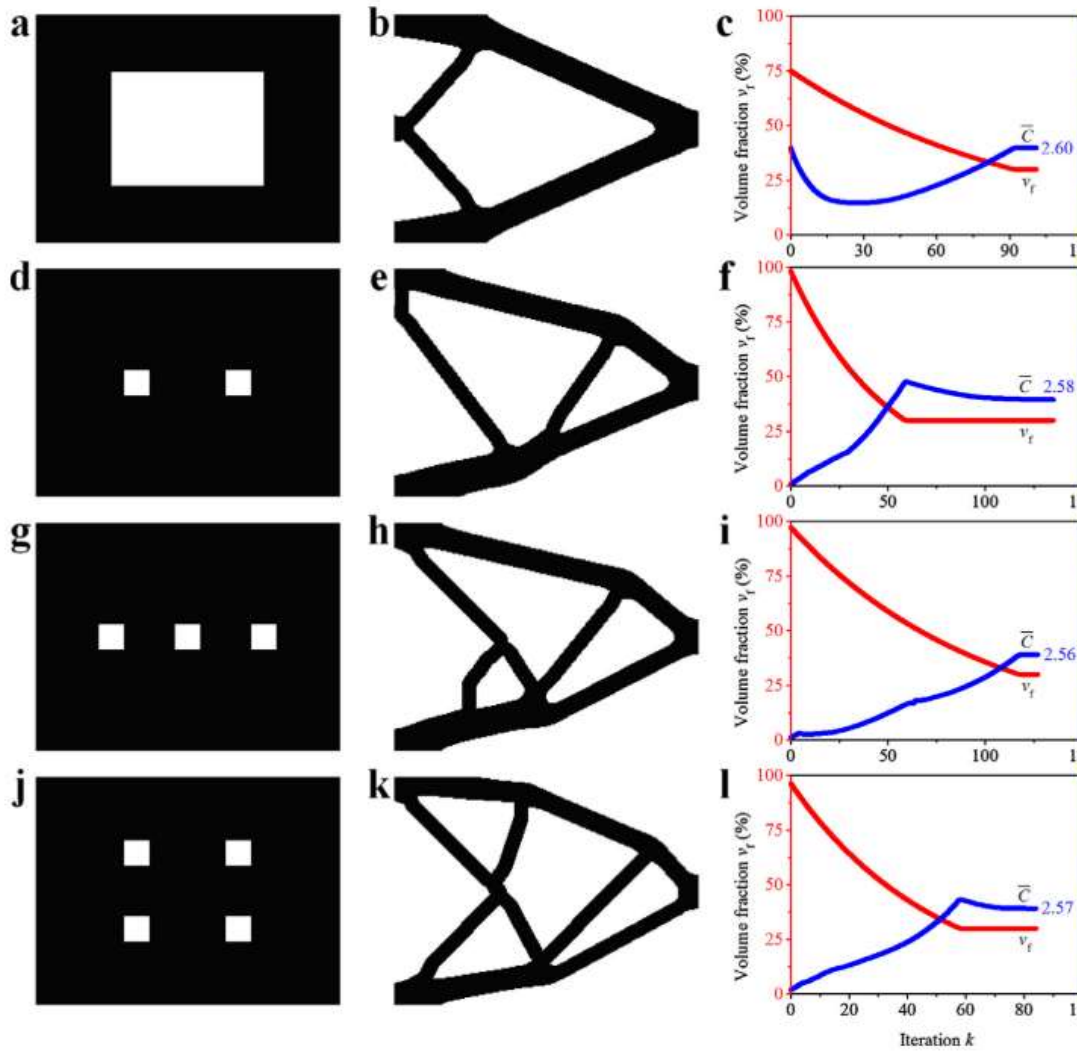


Fig. 16 - Influence of the number of the holes on the optimized design of a cantilever beam. The initial design, optimized design, and evolution histories of volume fraction and normalized compliance of the beam are plotted from left to right for four different cases (a)-(c), (d)-(f), (g)-(i), (j)-(l) [19].

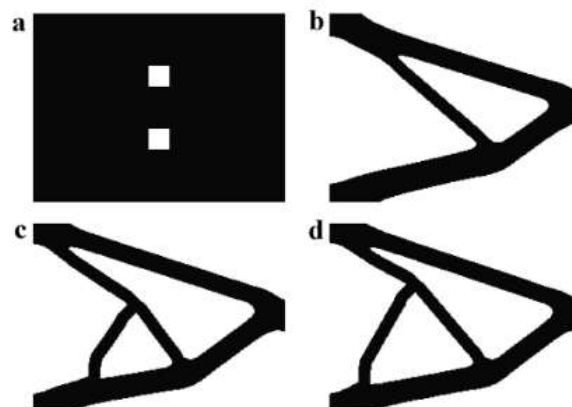


Fig. 17 - Influence of the hole size on the optimized design on a cantilever beam. (a) Two interior holes are included in the initial design. In the optimization, each hole is required to be not smaller than 0 for (b), 1/20 for (c), and 1/10 for (d) of the volume of the design domain [19].

Another recent study was proposed by Liu [23]. In this work a fully parallel parameterized level set method [24, 25] with compactly supported radial basis functions (CSRBFs) [26–28] is developed based on both the uniform and non-uniform structured meshes, in order to produce large-scale or high-resolution structural topology optimization design. It was found that, in the optimized structures, the thin sheet-like components gradually replace the truss-like ones when refining the mesh, Fig. 19. The parameterization process of the level set function will become faster as long as the non-uniformity of mesh is not very high and the supported radius of CSRBF is small enough. It was documented that more than 80% of the total computing time is always consumed for solving the structural state equations during the finite element analysis.

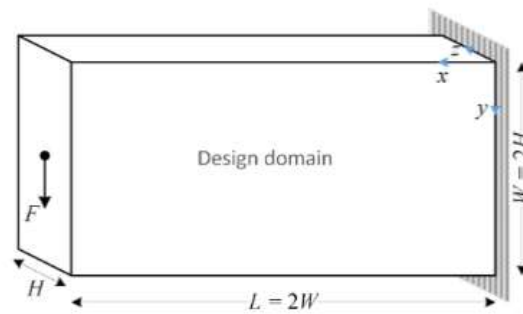


Fig. 18 - Three-dimensional cantilever beam model and its load and displacement boundary conditions [23].

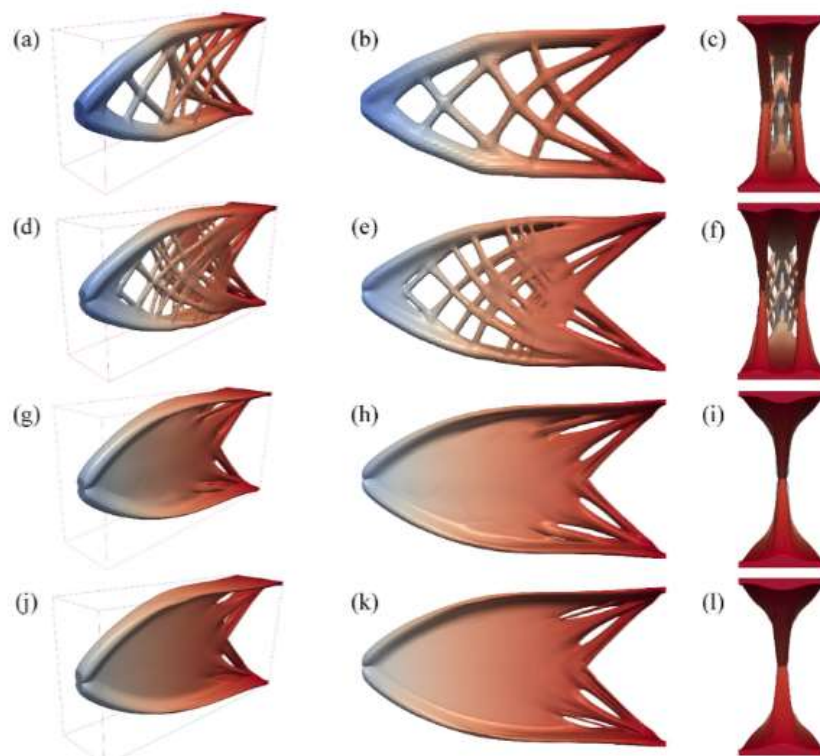


Fig. 19 - Optimized results based on four uniform structured meshes. All the results are colored by the displacement field in the y direction [23].

THESIS DEVELOPMENT

4 Numerical examples

In this chapter it will be presented three numerical examples in order to validate the structural optimization process implemented in the software FEMAS. The first two numerical examples are benchmark models such as beams, plates and frames, the analysis of these will permit to acquire autonomy in the use of the proposed software and becoming familiar with different types of numerical methods and analyses. The third numerical example is an industry application. The primary softwares used were FEMAP (Siemens PLM Software, student version), which provides drawing tools to create a model and to construct the respective mesh, and FEMAS, a Finite Element and Meshless Analysis Software (cmech.webs.com), which is a freeware academic software capable to analyse models using either the FEM or meshless methods.

4.1 Numerical example 1: Cantilever Beam

The first numerical example is a cantilever beam, fixed on the left side and loaded with a concentrated force (F) of 3 kN at the middle of the right side, Fig. 20. The problem domain has a rectangular shape with 160 mm of length, 100 mm of height and 1 mm of thickness.

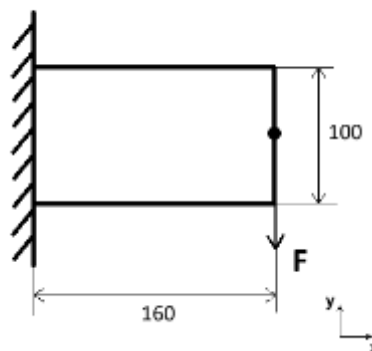


Fig. 20 - Cantilever beam model.

The elastic material properties are chosen as Young's modulus (E) = 207 GPa, Poisson's ratio (ν) = 0.3 and Yield Stress (σ_y) = 200 MPa.

The results documented in the literature generally resemble the shape of Fig. 21.

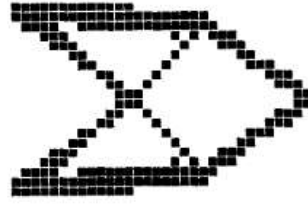


Fig. 21 – Cantilever beam optimized shape obtained from literature [29].

4.1.1 Domain discretization type influence

To study the influence of the domain discretization in the optimization process, a structural optimization analysis is performed considering a regular mesh of 640 quadrilateral elements, Fig. 22 (a), and another one using a regular mesh of 1280 triangular elements, Fig. 22 (b). In this study, the optimization method used is FEM, considering a linear static plane stress approach and the optimization criterion was the minimization of the VM effective stress.

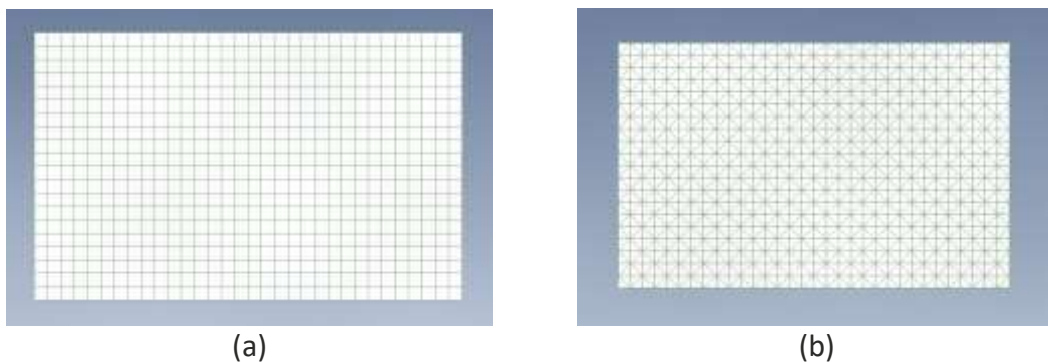

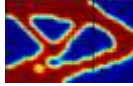
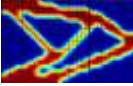
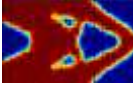

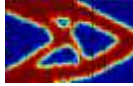
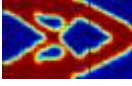
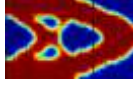

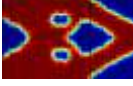
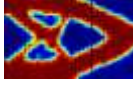
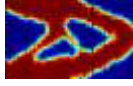
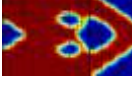
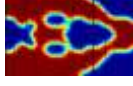
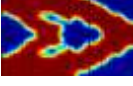





Fig. 22 – Cantilever beam regular mesh using 640 quadrilateral elements (a) and 1280 triangular elements (b).

In Table 1, it is presented the optimal solutions along with the iteration at each solution, considering DR of 4%, 5% and 10% for both types of domain discretization. As expected, the discretization using triangular elements, for the same number of divisions presents the double of elements as the one using quadrilateral elements. Rather than that, both meshes were capable of producing good structural shapes, however, the one with quadrilateral elements got optimal shapes closer to the one documented in literature.

Table 1 – Cantilever beam optimized solutions using quadrilateral and triangular elements for DR of 4%, 5% and 10%.

| DR | Quadrilateral Elements | | | Triangular Elements | | |
|-----|---|---|---|--|---|---|
| 4% |  |  |  |  |  |  |
| | 25 | 56 | 83 | 12 | 20 | 80 |
| 5% |  |  |  |  |  |  |
| | 18 | 30 | 35 | 9 | 23 | 43 |
| 10% |  |  |  |  |  |  |
| | 4 | 8 | 10 | 3 | 4 | 5 |

4.1.2 Mesh influence and optimization parameters

In order to obtain an optimal solution like the one documented in the literature, Fig. 21, it is important to analyse how the mesh and optimization parameters influence the optimal solutions. To study this, a structural optimization is performed and analysed using FEM, RPIM and NNRPIM, considering a linear static plane stress approach and the optimization criterion was the minimization of the VM effective stress. In FEM analysis, a classic FEM formulation is used considering four node quadrilateral elements. In relation to RPIM, sixteen nodes inside the influence domain are considered and a Gaussian integration is performed using quadrilateral integration cells with 2×2 integration points. As in the NNRPIM, second-degree influence cells and a full integration are considered. Concerning the RPI shape functions in RPIM and NNRPIM, the following parameters are assumed: $c=0.0001$, $p=0.9999$ and constant polynomial basis.

The structural optimization analysis is performed considering a regular mesh of 693 nodes, Fig. 23 (a), and a regular mesh of 2665 nodes, Fig. 23 (b). Also, the analysis is performed considering DR of 2%, 3%, 4%, 5% and 10%. To avoid stress concentrations, that may lead to inaccurate solutions, the load of 3 kN is distributed over three nodes.

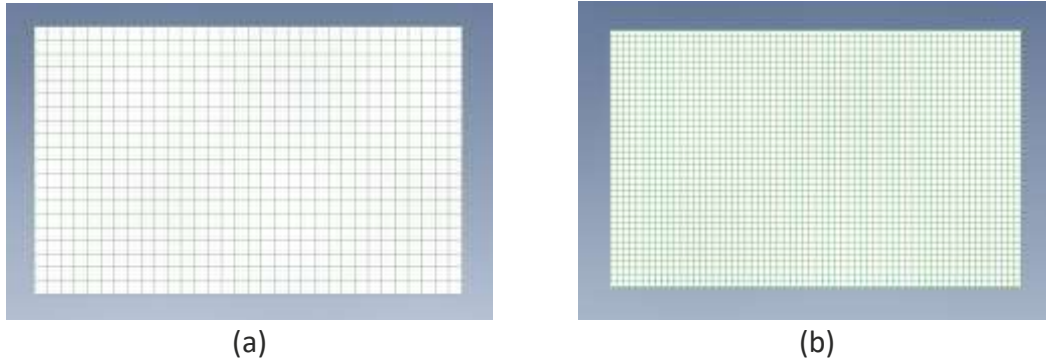


Fig. 23 – Cantilever beam regular quadrilateral mesh using 693 nodes (a) and 2665 nodes (b).

In Table 2 and Table 3, is presented the solutions obtained from the structural optimization analysis using a regular mesh of 693 and 2665 nodes respectively, along with the iteration at each solution and the respective mass reduction.

Table 2 – Cantilever beam structural optimization solutions using FEM, RPIM and NNRPIM and DR of 2%, 3%, 4%, 5% and 10% for a regular quadrilateral mesh of 693 nodes.







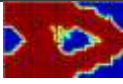

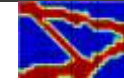






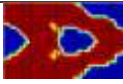
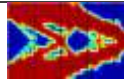
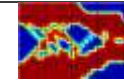
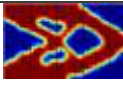
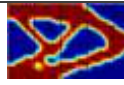
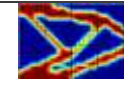


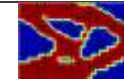
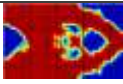
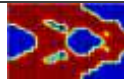
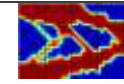

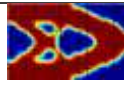
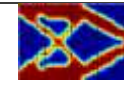
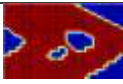

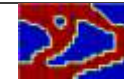
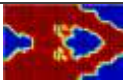
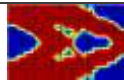
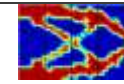
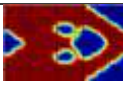

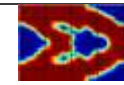
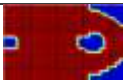
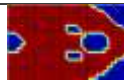
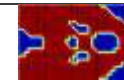
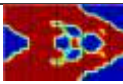
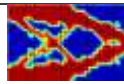
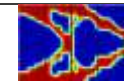






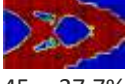








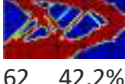

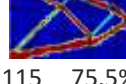







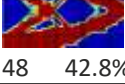
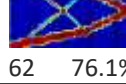

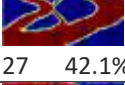






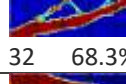






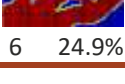
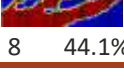
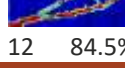
| DR | Optimization Method | Structural Optimization Solutions | | | | | | | | |
|-----|---------------------|---|--|---|----|-------|-----|-------|-----|-------|
| 2% | FEM |  |  |  | 5 | 8.2% | 10 | 13.2% | 12 | 13.8% |
| | RPIM |  |  |  | 5 | 6.1% | 15 | 10.7% | 24 | 15.8% |
| | NNRPIM |  |  |  | 20 | 26.9% | 120 | 40.3% | 145 | 62.5% |
| 3% | FEM |  |  |  | 15 | 29.4% | 35 | 39.6% | 55 | 41.7% |
| | RPIM |  |  |  | 10 | 12.2% | 15 | 15.5% | 21 | 25% |
| | NNRPIM |  |  |  | 18 | 30.5% | 30 | 38.1% | 53 | 37.3% |
| 4% | FEM |  |  |  | 25 | 41.3% | 56 | 48.8% | 83 | 63.7% |
| | RPIM |  |  |  | 42 | 35.6% | 63 | 41.4% | 85 | 40.9% |
| | NNRPIM |  |  |  | 10 | 29.1% | 17 | 35.5% | 53 | 48.2% |
| 5% | FEM |  |  |  | 18 | 45.4% | 30 | 37.9% | 35 | 54.9% |
| | RPIM |  |  |  | 30 | 23.9% | 37 | 34.4% | 58 | 48.5% |
| | NNRPIM |  |  |  | 16 | 31.2% | 20 | 31.6% | 28 | 59.3% |
| 10% | FEM |  |  |  | 4 | 27.2% | 8 | 40.9% | 10 | 35.9% |
| | RPIM |  |  |  | 3 | 16.5% | 4 | 22% | 5 | 25.7% |
| | NNRPIM |  |  |  | 6 | 32.2% | 13 | 47.9% | 22 | 63.1% |

Table 3 - Cantilever beam structural optimization solutions using FEM, RPIM and NNRPIM and DR of 2%, 3%, 4%, 5% and 10% for a regular quadrilateral mesh of 2665 nodes.



























| DR | Optimization Method | Structural Optimization Solutions | | | | | | | | |
|-----|---------------------|---|--|---|----|-------|-----|-------|-----|-------|
| 2% | FEM |  |  |  | 29 | 26.4% | 45 | 30.6% | 52 | 27.8% |
| | RPIM |  |  |  | 44 | 31% | 90 | 39.7% | 114 | 50.1% |
| | NNRPIM |  |  |  | 45 | 37.7% | 104 | 77.4% | 165 | 79.2% |
| 3% | FEM |  |  |  | 18 | 25.3% | 48 | 35.5% | 101 | 45.1% |
| | RPIM |  |  |  | 17 | 26.8% | 33 | 35.7% | 52 | 43.9% |
| | NNRPIM |  |  |  | 62 | 42.2% | 85 | 49.8% | 115 | 75.5% |
| 4% | FEM |  |  |  | 21 | 29.9% | 36 | 39.4% | 57 | 54.7% |
| | RPIM |  |  |  | 25 | 34.8% | 34 | 38.4% | 57 | 45.5% |
| | NNRPIM |  |  |  | 27 | 39.1% | 48 | 42.8% | 62 | 76.1% |
| 5% | FEM |  |  |  | 18 | 35.4% | 27 | 42.1% | 55 | 63.4% |
| | RPIM |  |  |  | 9 | 24.9% | 41 | 44.2% | 63 | 52.5% |
| | NNRPIM |  |  |  | 12 | 30.4% | 28 | 48.4% | 32 | 68.3% |
| 10% | FEM |  |  |  | 6 | 37.9% | 8 | 39.5% | 10 | 58.3% |
| | RPIM |  |  |  | 5 | 24.5% | 8 | 33.7% | 11 | 40.2% |
| | NNRPIM |  |  |  | 6 | 24.9% | 8 | 44.1% | 12 | 84.5% |

After obtaining the structural optimization solutions presented in Table 2 and Table 3, a summary of the optimal solutions that reached the shape of the one reported in the literature is shown in Table 4. As it can be seen, some analyses did not reach the optimal shape reported in literature unlike others. Considering a mesh with 2665 nodes over a mesh of 693 nodes results in a higher number of solutions. However, both meshes were able to produce good solutions under specific parameters and numerical methods.

When considering a mesh with 693 nodes, it is possible to verify that proper solutions could not be achieved with DR of 2% and 3% with any of the numerical methods. Since in these cases the DR is too low, this can explain the fact that the algorithm cannot manage to evolve the structure towards an optimal solution and therefore stopping the process at early iterations. Beyond this, no optimal solutions were obtained when using the RPIM for any DR. However, when considering 4%, 5% and 10% DR, FEM and NNRPIM were able to achieve remarkable solutions. Even though, the best results were obtained when considering a DR of 5% for both FEM and NNRPIM. With these parameters, both methods were able to produce an optimal solution between 55% and 60% mass reduction from its original structure and a shape identical to the one referred in the literature. Although both FEM and NNRPIM produced optimal solutions, a smoothest shape is obtained with FEM rather than NNRPIM.

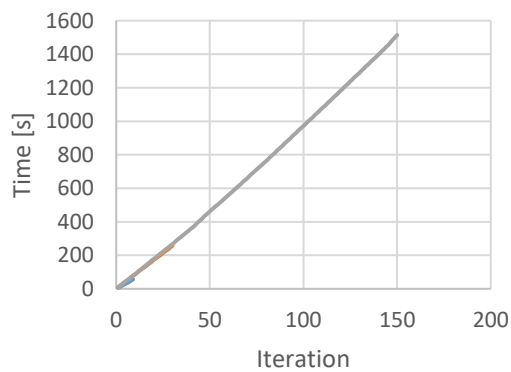
On the other hand, when using a mesh with 2665 nodes, proper solutions were achieved when using a DR of 2% and 3%, yet at later iterations. Nonetheless, the better and higher number of solutions were obtained for a DR between 4% and 5%, reaching mass reductions around 75% in some cases. When comparing the numerical methods, it is important to refer that solutions were obtained when using RPIM even though in lower number, and both FEM and NNRPIM can achieve optimal solutions over a wider variety of DR. Lastly, this mesh produces more refined shapes in comparison with the mesh of 693 nodes.

Table 4 – Summary of the cantilever beam optimal solutions that reached the shape referred in literature.

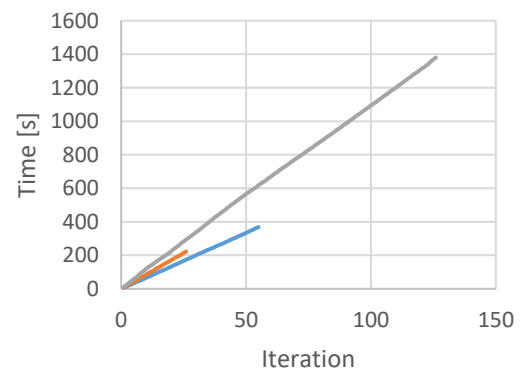
| | | 693 nodes | | | | | | | |
|--------|--|--|--|--|--|---|---|---|---|
| | | 2% | 3% | 4% | 5% | 10% | | | |
| FEM | | - | - |  25 |  18 |  30 |  35 |  4 |  8 |
| RPIM | | - | - | - | - | | | - | |
| NNRPIM | | - | - |  17 |  20 |  28 |  13 |  22 | |
| | | 2665 nodes | | | | | | | |
| | | 2% | 3% | 4% | 5% | 10% | | | |
| FEM | | - |  101 |  36 |  57 |  27 |  55 |  10 | |
| RPIM | |  114 | - | - | |  63 | | - | |
| NNRPIM | |  45 |  104 |  165 | - |  48 |  62 |  32 |  12 |

4.1.3 Computational Time

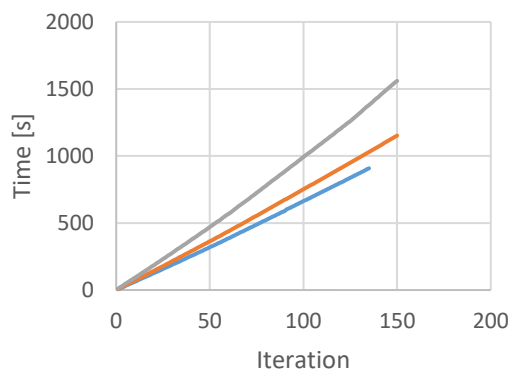
In this chapter it is covered the impact of each numerical method regarding the computational time. In Fig. 24 and Fig. 25, it is shown the graphs that represent the computational time for the respective iteration, using 693 and 2665 nodes respectively. As it was expected, when optimizing a structure using a mesh with 2665 nodes over a mesh with 693 nodes, for the same iteration it takes around 5 times more. When comparing the numerical methods, FEM is the faster following RPIM and NNRPIM. As for the influence of the DR, no major differences are observed. Therefore, the computational time is not affected when using different percentages of DR. However, when observing Fig. 26, it is possible to notice that using a higher DR, permits to obtain optimal solutions earlier.



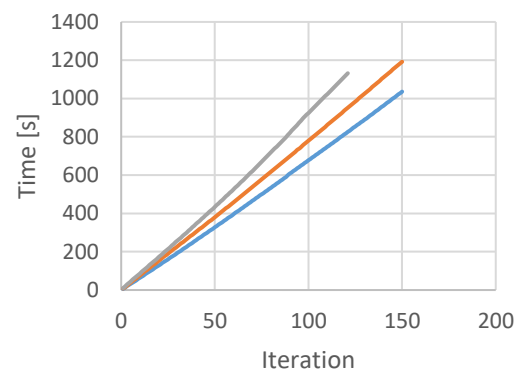
a)



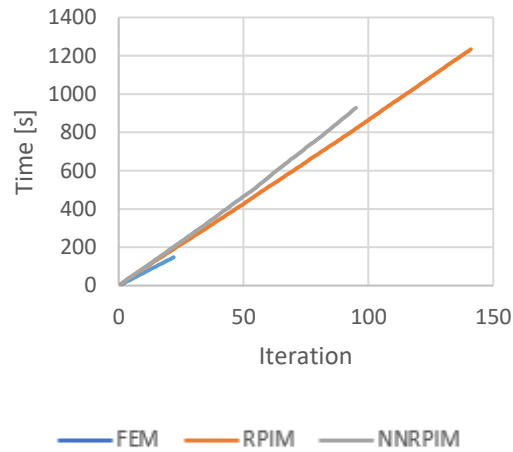
b)



c)

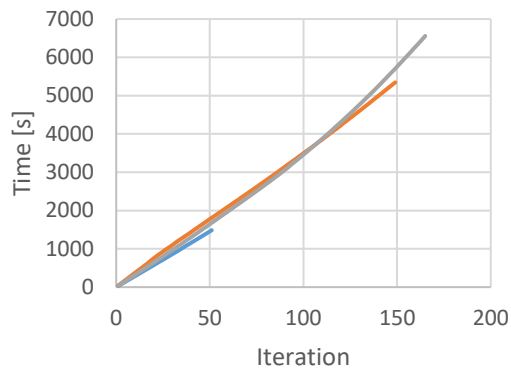


d)

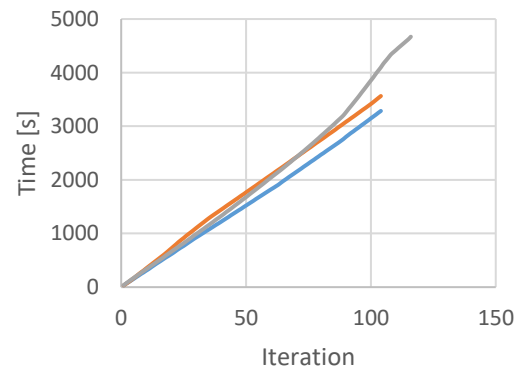


e)

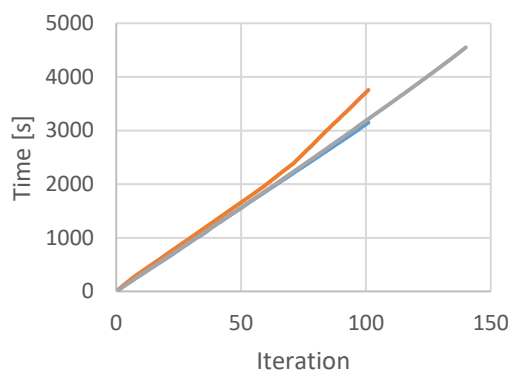
Fig. 24 – Cantilever beam computational time per iteration using a regular quadrilateral mesh of 693 nodes, FEM, RPIM and NNRPIM for DR of 2% (a), 3% (b), 4% (c), 5% (d) and 10% (e).



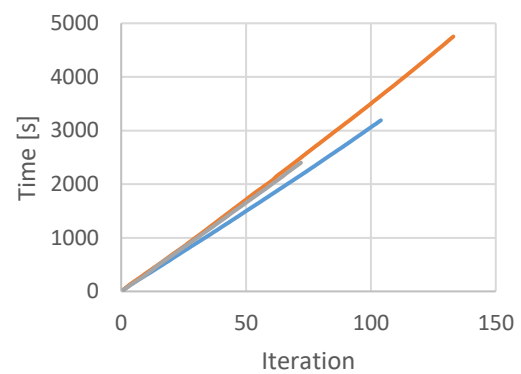
a)



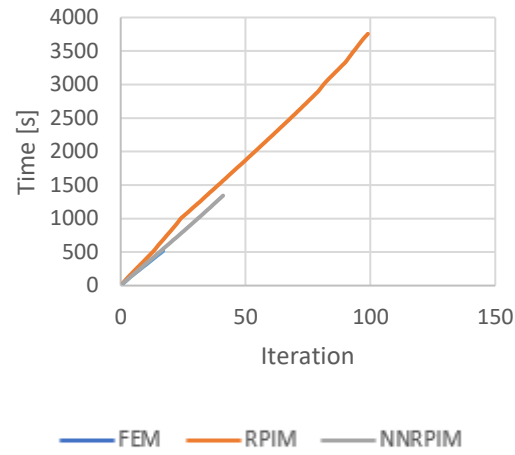
b)



c)

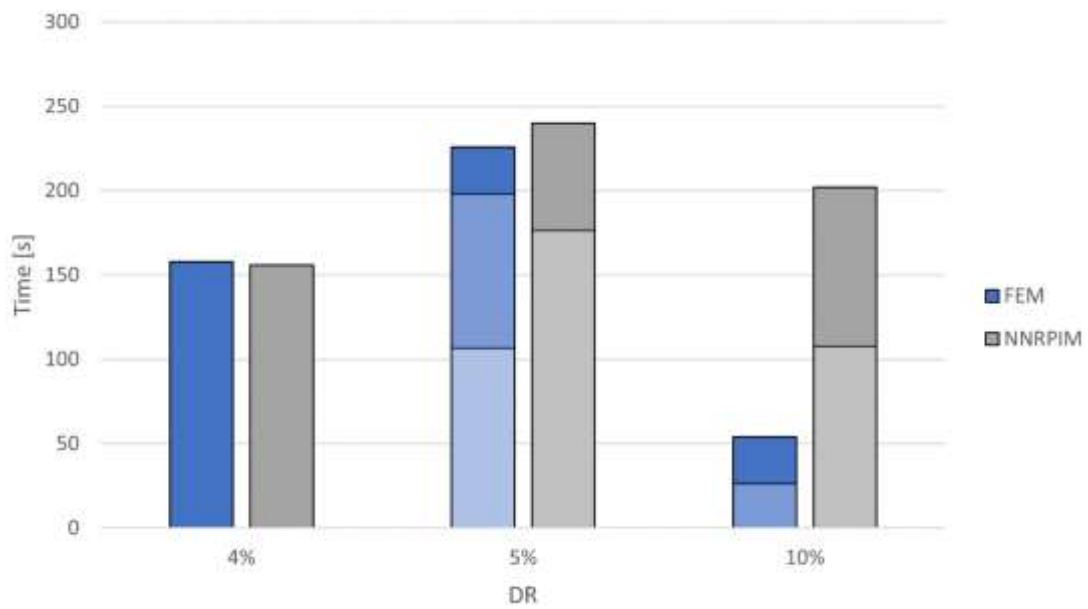


d)

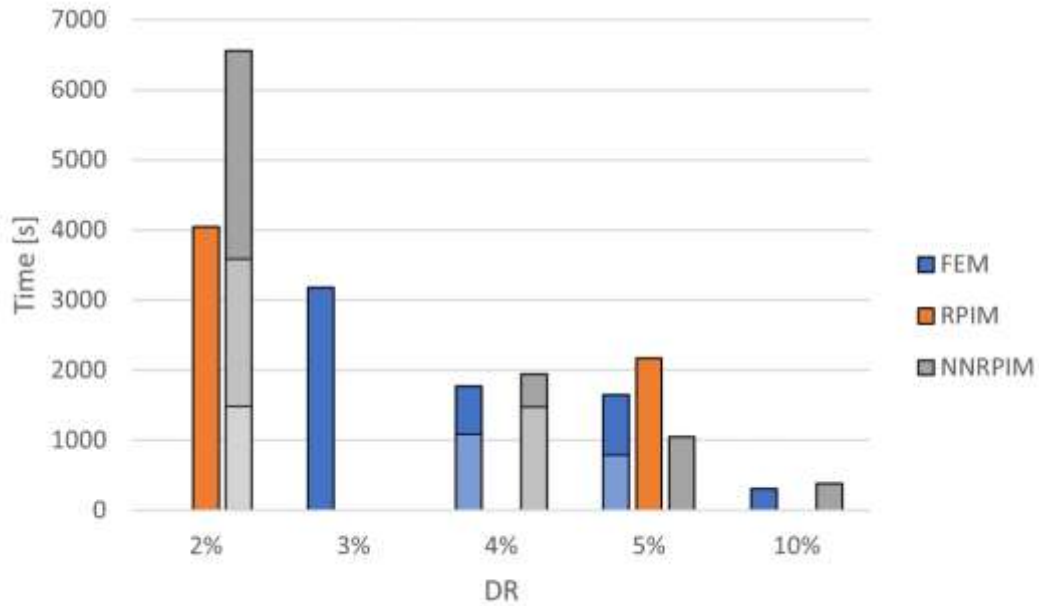


e)

Fig. 25 - Cantilever beam computational time per iteration using a regular quadrilateral mesh of 2665 nodes, FEM, RPIM and NNRPIM for DR of 2% (a), 3% (b), 4% (c), 5% (d) and 10% (e).



a)



b)

Fig. 26 – Cantilever beam computational time per DR using a regular quadrilateral mesh of 693 nodes (a) and 2665 nodes (b), for solutions that reached the shape referred in literature.

4.1.4 Cantilever Beam Variant

After obtaining the results of the structural optimization for the standard cantilever beam, the idea of how holes in the structure would affect the process of optimization arise. To study this, two holes were implemented in the design domain of the structure, Fig. 27. Firstly, a mesh of 1294 triangular elements randomly distributed was created, Fig. 28 (a). Then a structural optimization analysis was performed using FEM and a DR of 5%, obtaining the structure present in Fig. 28 (b).

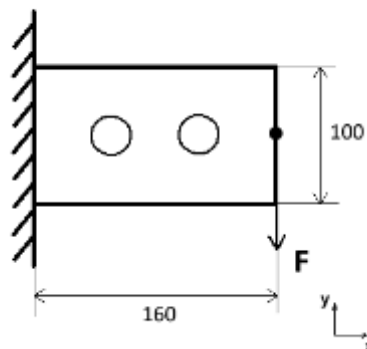


Fig. 27 – Cantilever beam model variant.

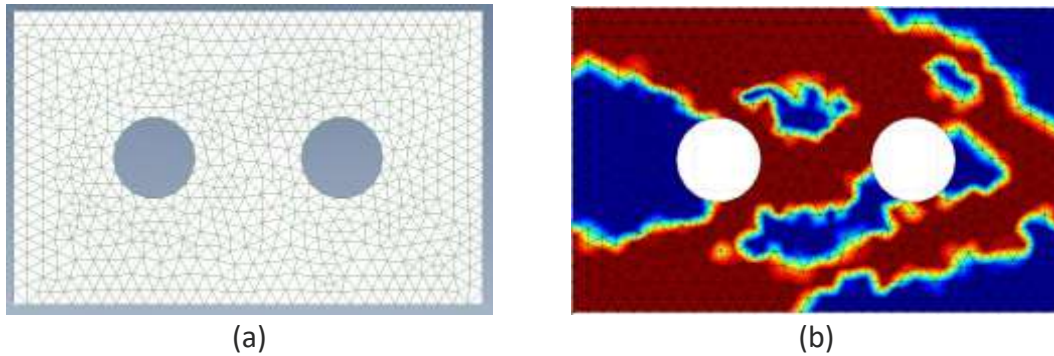


Fig. 28 – Cantilever beam variant irregular mesh of 1294 triangular elements (a) and its optimization solution (b).

Since this structure was not expected, a new structural optimization analysis was performed using FEM, RPIM and NNRPIM, but this time using a different mesh of 1020 triangular elements uniformly distributed through the domain, Fig. 29. The optimal solutions obtained from this optimization, Fig. 30, shows that using a uniformly mesh over a randomly distributed one has a significant impact on the results obtained, once a randomly distributed mesh is not capable to produce well-defined structures.

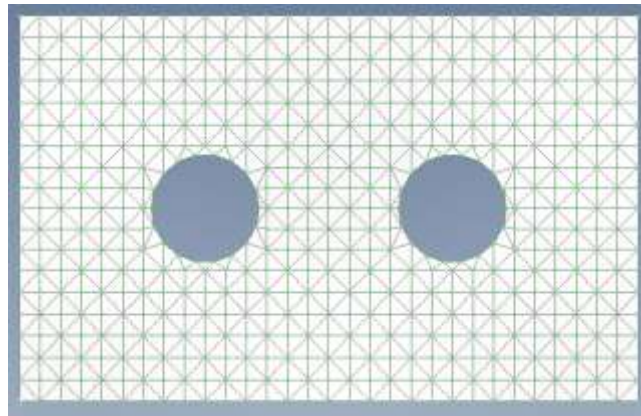


Fig. 29 – Cantilever beam variant regular mesh of 1020 triangular elements.

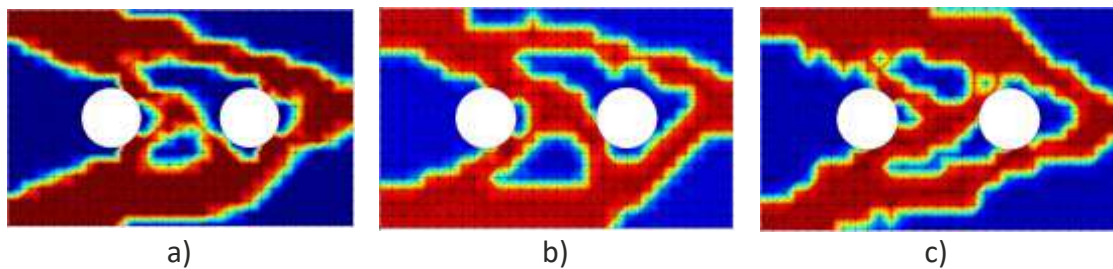


Fig. 30 – Cantilever beam variant optimized solutions using FEM (a), RPIM (b) and NNRPIM (c) using a regular mesh of 1020 triangular elements.

Comparing these optimal solutions with the ones obtained without the holes in the structure, it is possible to see a detour from the zone where the trusses would normally cross, since the program had to adjust its optimization due to the presence of the holes in the new structure. Furthermore, all numerical methods were able to produce identical solutions, and as for the percentage of mass reduction the implemented holes did not make a significant impact, as 50% mass reduction was reached in every method.

4.2 Numerical Example 2: Simply supported Beam

The following numerical example is a simply supported beam, with the two bottom corners fixed and a concentrated force (F) of 1 kN loaded at the center of the bottom surface, Fig. 31. The problem domain has a rectangular shape with 10 m of length, 5 m of height and 1 m of thickness.

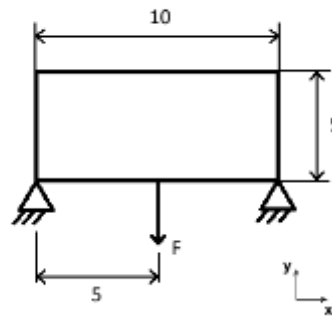


Fig. 31 – Simply supported beam model.

The elastic material properties are chosen as Young's modulus (E) = 100 GPa, Poisson's ratio (ν) = 0.3 and Yield Stress (σ_y) = 100 MPa.

The results documented in the literature generally resemble the shape of Fig. 32. This structure was obtained with approximately 20 % of the initial volume and it was obtained with a discretization of 25 x 50 four-node elements.



Fig. 32 – Simply supported beam optimized shape obtained from literature [30].

4.2.1 Mesh influence and optimization parameters

As in the previous numerical example (Cantilever Beam), several structural optimization analyses are performed using FEM, RPIM and NNRPIM, considering a linear static plane stress approach and the VM effective stress chosen as the optimality criterion. The numerical method formulations and parameters used in this example are equal to the previous example as well.

The structural optimization analysis is performed considering a regular mesh of 1326 nodes, Fig. 33 (a), and a regular mesh of 5151 nodes, Fig. 33 (b). Also, the analysis is performed considering DR of 4%, 5% and 10%. To avoid stress concentrations, that may lead to inaccurate solutions, the load of 1 kN is distributed over five nodes.

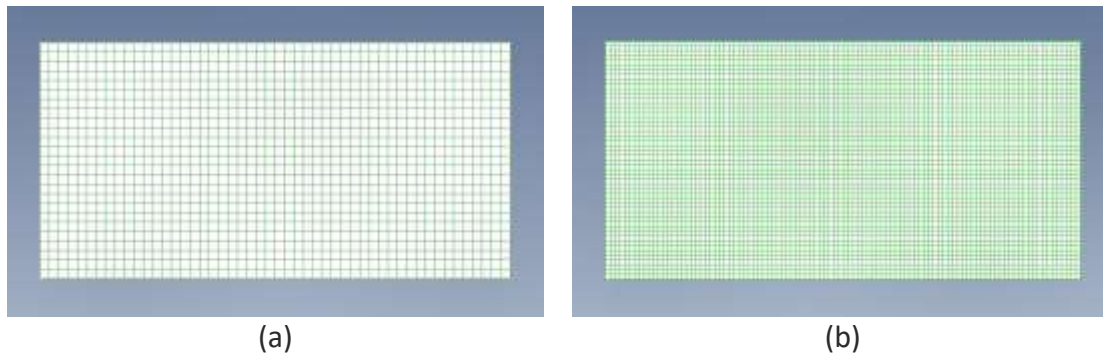


Fig. 33 – Simply supported beam regular quadrilateral mesh using 1326 nodes (a) and 5151 nodes (b).

In Table 5 and Table 6, is presented the solutions obtained from the structural optimization analysis using a regular mesh of 1326 and 5151 nodes respectively, along with the iteration at each solution and the respective mass reduction.

Table 5 – Simply supported beam structural optimization solutions using FEM, RPIM and NNRPIM and DR of 4%, 5% and 10% for a regular quadrilateral mesh of 1326 nodes.

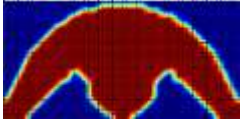
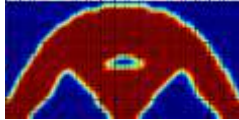
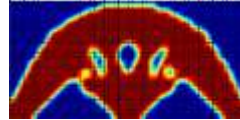
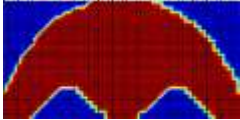
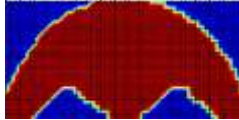
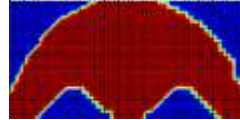
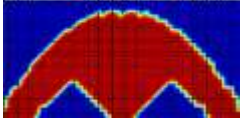
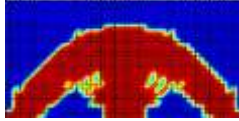
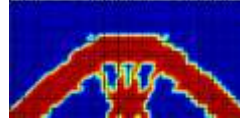
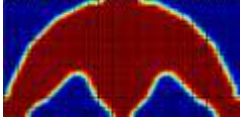
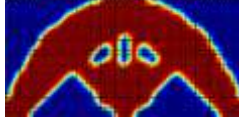




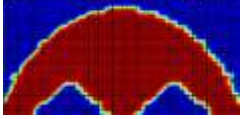

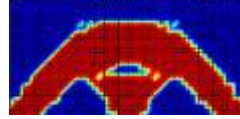

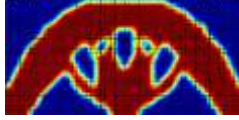
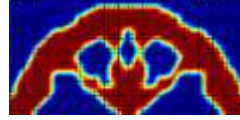
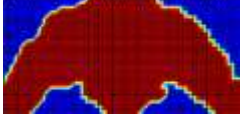


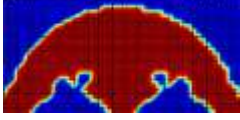
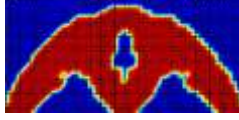
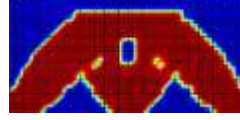



























| DR | Optimization Method | Structural Optimization Solutions | | | | | | | | | |
|-----|---------------------|---|--|---|--|---|-------|-------|-------|-------|-------|
| 4% | FEM |  |  |  | 68 | 44.3% | 102 | 45.5% | 107 | 44.7% | |
| | | RPIM |  |  |  | 33 | 32.7% | 49 | 32.4% | 54 | 32.7% |
| | | | NNRPIM |  |  |  | 107 | 48.4% | 181 | 55.3% | 199 |
| | FEM | | |  |  |  | 17 | 40.5% | 21 | 43.4% | 73 |
| | | RPIM | |  |  |  | 13 | 31.3% | 29 | 33% | 50 |
| | | | NNRPIM |  |  |  | 46 | 45% | 87 | 54.6% | 141 |
| 10% | FEM | | |  |  |  | 23 | 45.7% | 25 | 44.8% | 46 |
| | | RPIM | |  |  |  | 6 | 31.2% | 38 | 41.8% | 43 |
| | | | NNRPIM |  |  |  | 15 | 45.3% | 17 | 50.9% | 18 |

Table 6 - Simply supported beam structural optimization solutions using FEM, RPIM and NNRPIM and DR of 4%, 5% and 10% for a regular quadrilateral mesh of 5151 nodes.




















| DR | Optimization Method | Structural Optimization Solutions | | | | | | | | | |
|-----|---------------------|---|--|---|---|-------|-------|-------|-------|-------|-------|
| 4% | FEM |  |  |  | 52 | 40.9% | 85 | 43% | 91 | 43.7% | |
| | |  |  |  | 38 | 35.6% | 78 | 41.8% | 93 | 40.7% | |
| | |  |  |  | 49 | 52.9% | 62 | 53.5% | 80 | 56.7% | |
| | 5% | FEM |  |  |  | 65 | 46.3% | 76 | 43.4% | 81 | 44.6% |
| | | |  |  |  | 52 | 38.3% | 78 | 41.9% | 84 | 38.8% |
| | | |  |  |  | 56 | 58.9% | 82 | 61.9% | 94 | 65.3% |
| 10% | FEM |  |  |  | 9 | 35.9% | 11 | 38.6% | 13 | 44.4% | |
| | |  |  |  | 15 | 47.4% | 16 | 45.8% | 20 | 46.7% | |
| | |  |  |  | 11 | 42.5% | 12 | 45.6% | 13 | 48.7% | |

In Table 7 is presented a summary of the optimal solutions that reached the shape documented in the literature. Observed the results, both meshes were able to produce optimal solutions with a similar shape to the one reported in the literature, however the mesh with 5151 nodes produces a higher number of optimal solutions over the mesh with 1326 nodes.

Considering a mesh with 1326 nodes, it can be noticed that the algorithm struggles to remove material inside the structure, incapacitating the structure to reach shapes similar to the one referred in the literature. Nonetheless, proper solutions were obtained when using FEM, being that the better and higher number of solutions were obtained using a DR of 10%. Important to refer that RPIM could not achieve proper solutions, in contrary of NNRPIM that achieved a proper solution when using a DR of 4% although at a later iteration.

For a mesh with 5151 nodes, a higher number of proper and well-defined solutions is obtained. When using this mesh instead of the previous with 1326 nodes, it is possible to verify that the algorithm can remove material inside the structure in every case. Whilst the algorithm removed material inside the structure when using RPIM, this was not sufficient as it did not achieve coherent solutions. Both FEM and NNRPIM were able to achieve proper solutions for all DR, yet the higher number of solutions were obtained for a DR of 5%.

Table 7 - Summary of the simply supported beam optimal solutions that reached the shape referred in literature.

| | | 1326 nodes | | | | |
|--------|--|--|---|---|---|---|
| | | 4% | 5% | 10% | | |
| FEM | |  107 |  21 |  23 |  25 |  46 |
| RPIM | | - | - | - | | |
| NNRPIM | |  199 | - | - | | |
| | | 5151 nodes | | | | |
| | | 4% | 5% | | 10% | |
| FEM | |  91 |  65 |  76 |  81 |  13 |
| RPIM | | - | - | | - | |
| NNRPIM | |  49 |  62 |  80 |  56 |  82 |
| | | | |  94 |  12 |  13 |

4.2.2 Computational Time

As in the cantilever beam example, it is possible to conclude from Fig. 34 and Fig. 35, that higher mesh density has a high impact on the computational time. Regarding the numerical methods, the same pattern as in the cantilever beam example can be seen, being NNRPIM the numerical method that takes more time per iteration followed by RPIM and FEM. However, when using the mesh with 5151 nodes, a change can be observed as RPIM is the method that takes more time per iteration followed by FEM and NNRPIM. As for the DR influence, the same conclusions can be taken from the cantilever beam example, Fig. 36.

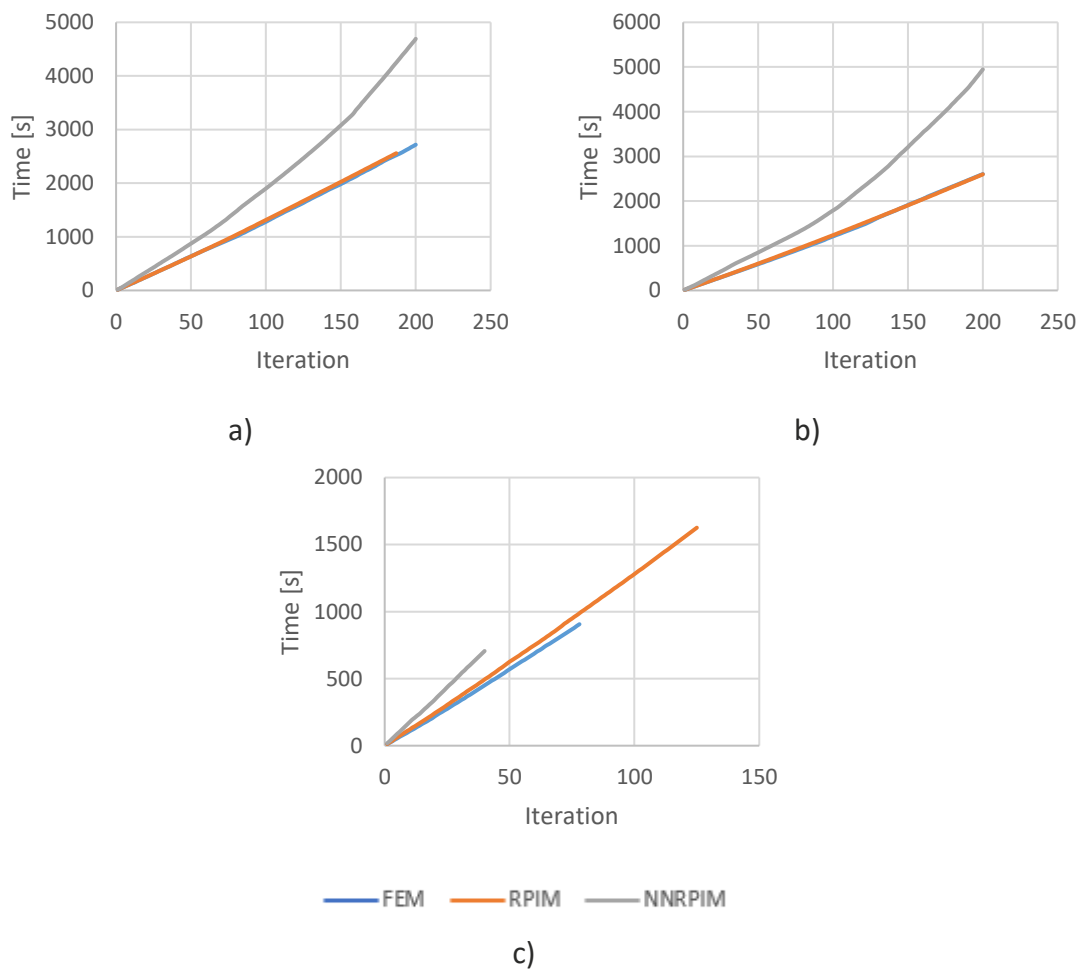


Fig. 34 – Simply supported beam computational time per iteration using a regular quadrilateral mesh of 1326 nodes, FEM, RPIM and NNRPIM for DR of 4% (a), 5% (b) and 10% (c).

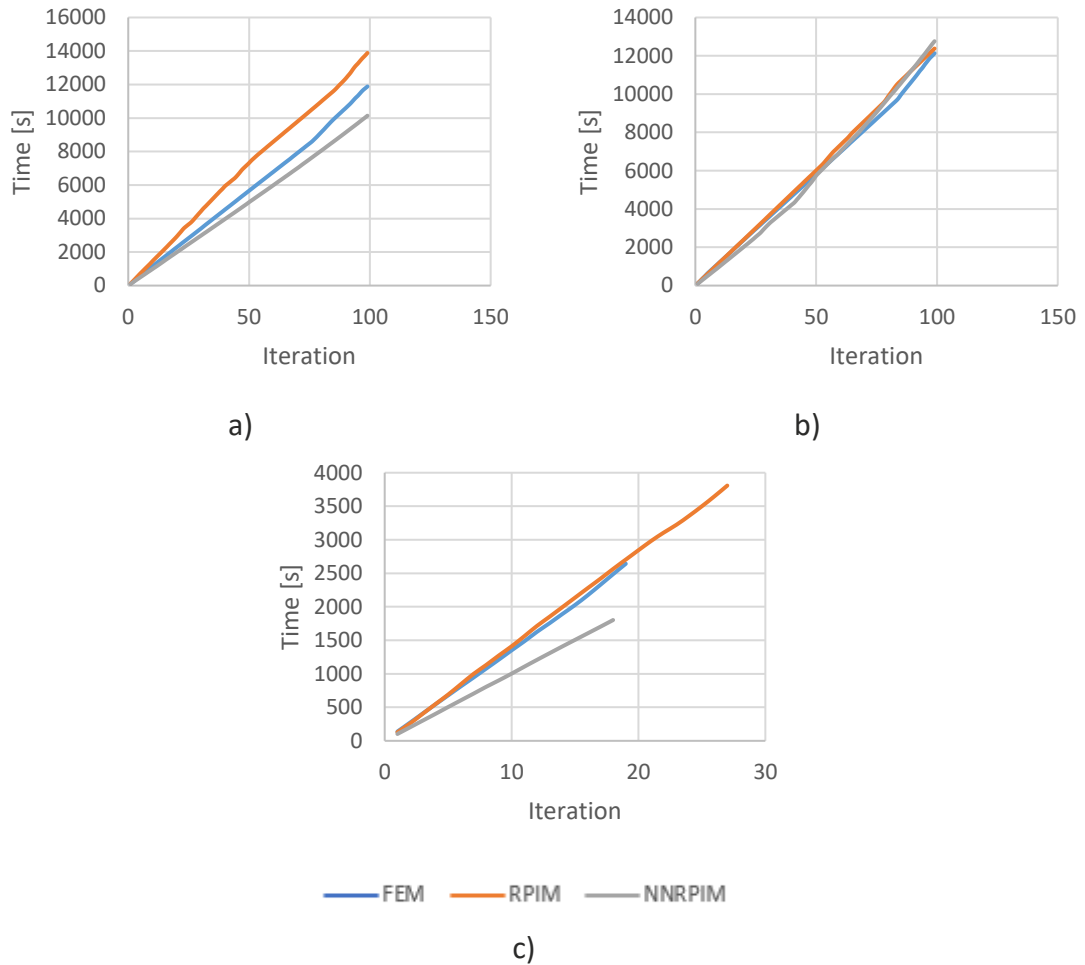


Fig. 35 - Simply supported beam computational time per iteration using a regular quadrilateral mesh of 5151 nodes, FEM, RPIM and NNRPIM for DR of 4% (a), 5% (b) and 10% (c).

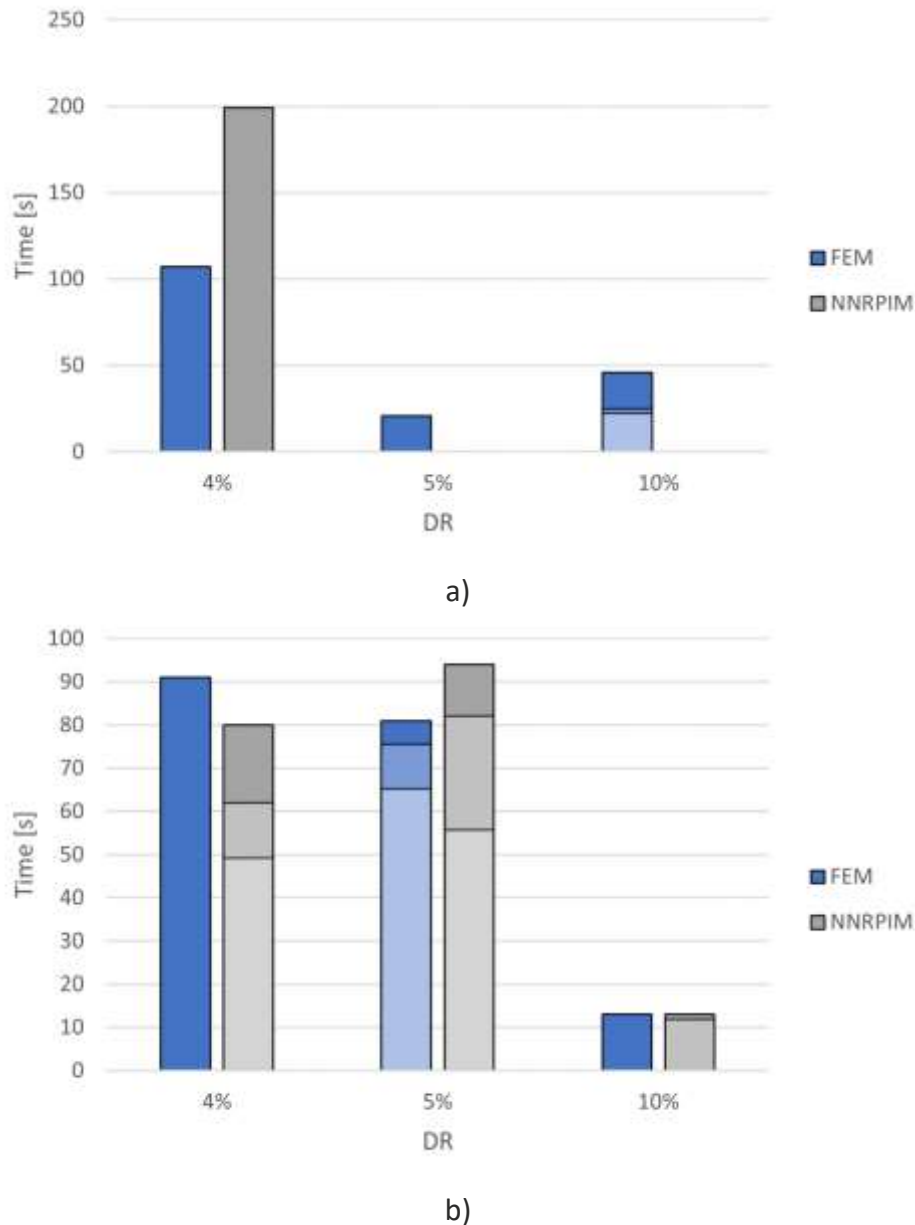
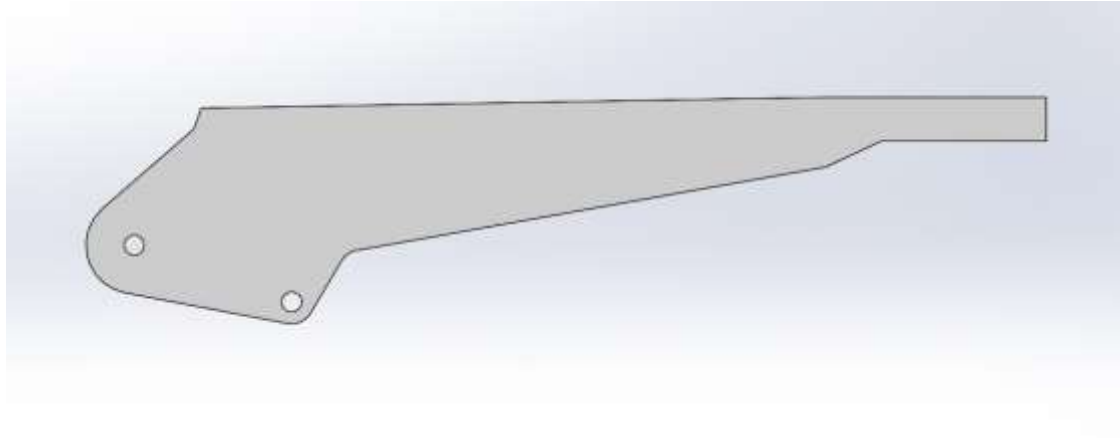


Fig. 36 – Simply supported beam computational time per DR using a regular quadrilateral mesh of 1326 nodes (a) and 5151 nodes (b), for solutions that reached the shape referred in literature.

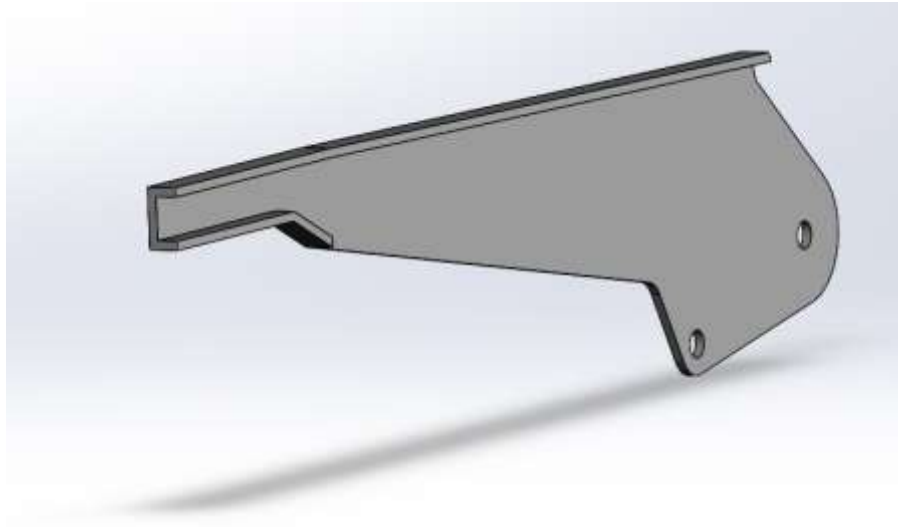
4.3 Handbrake Lever

The application of structural optimization to design industry parts is commonly used. Such computational technique is important since it increases the performance of structural parts, while granting less material usage which subsequently means lower prices to fabricate them.

In this chapter, structural optimization is implemented into a handbrake lever from a standard road car. As in benchmark examples, the structural optimization is performed using FEM, RPIM and NNRPIM, as well as its parameters and formulations. The analysis is performed considering DR of 4%, 5% and 10% for 2D and 5% for 3D model.



a)



b)

Fig. 38 – Handbrake lever 2D (a) and 3D (b) model.

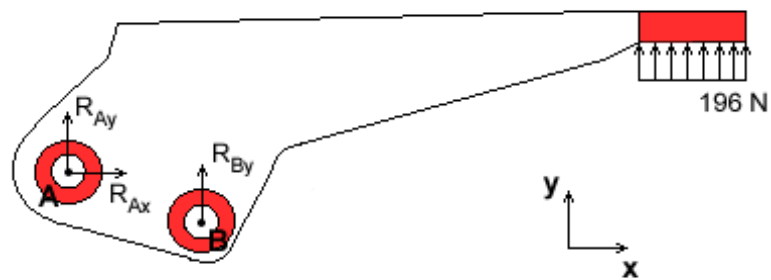

















Fig. 39 – Essential and natural boundary conditions applied to the handbrake lever.

4.3.1 2D

Firstly, a 2D structural optimization analysis is performed. The design domain is discretized by 1828 nodes and 3394 triangular elements. In Table 8, is presented the solutions obtained from the structural optimization analysis, along with the iteration at each solution and the respective mass reduction. From Table 8, it is possible to verify that under specific combinations of DR, all methods reached identical solutions. However, consistent and smoother solutions were obtained for a DR of 5%, achieving mass reductions around 50%.

Table 8 – Handbrake lever 2D model structural optimization solutions using FEM, RPIM and NNRPIM and DR of 4%, 5% and 10% for a mesh of 1828 triangular elements.




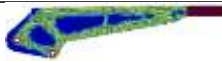
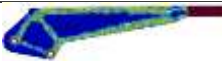
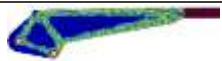

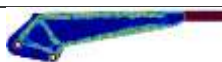
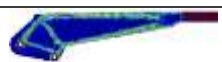
| DR | Optimization Method | Structural Optimization Solutions | | | | | |
|-----|---------------------|--|-------|--|-------|--|-------|
| 4% | FEM |  27 | 40.1% |  34 | 44% | | |
| | RPIM | 7 | | 3.4% | | | |
| | NNRPIM |  20 | 42.4% |  24 | 38.4% |  82 | 47.1% |
| 5% | FEM |  18 | 36.7% |  64 | 37.6% |  81 | 42.5% |
| | RPIM |  27 | 33.9% |  30 | 42% |  43 | 44.9% |
| | NNRPIM |  16 | 46.5% |  22 | 49.2% | | |
| 10% | FEM | 8 | | 42.4% | | | |
| | RPIM | 7 | | 29.4% | | | |
| | NNRPIM |  7 | 46.3% |  9 | 46.8% | | |

4.3.2 3D

Secondly, a 3D structural optimization analysis is performed. In this case, since the handbrake geometry is symmetrical along the plane Oxy, only half of the structure was analysed providing increased mesh density in the study. The design domain is discretized by 5183 nodes and 15397 tetrahedral elements. In Table 9, is presented the solutions obtained from the structural optimization analysis, along with the iteration at each solution and the respective mass reduction. From Table 9, optimal solutions like the ones obtained for 2D model can be obtained, with any of the numerical methods. With this optimization, mass reductions around 55% are achieved.

Although good solutions can be obtained using 3D models, the analysis of these ends up being inefficient due to the computational time being around twenty times higher than using 2D models, Fig. 40.

Table 9 - Handbrake lever 3D model structural optimization solutions using FEM, RPIM and NNRPIM and DR of 5% for a mesh of 15397 tetrahedral elements.

| DR | Optimization Method | Structural Optimization Solutions | | | | | | | | |
|----|---------------------|---|----|-------|--|----|-------|---|----|-------|
| 5% | FEM |  | 28 | 34.7% |  | 30 | 37.5% |  | 35 | 54.8% |
| | |  | 29 | 33.2% |  | 37 | 49.7% |  | 45 | 41.1% |
| | |  | 24 | 52.5% |  | 32 | 53.5% |  | 39 | 53.7% |
| | RPIM | | | | | | | | | |
| | | | | | | | | | | |
| | | | | | | | | | | |
| | NNRPIM | | | | | | | | | |
| | | | | | | | | | | |
| | | | | | | | | | | |

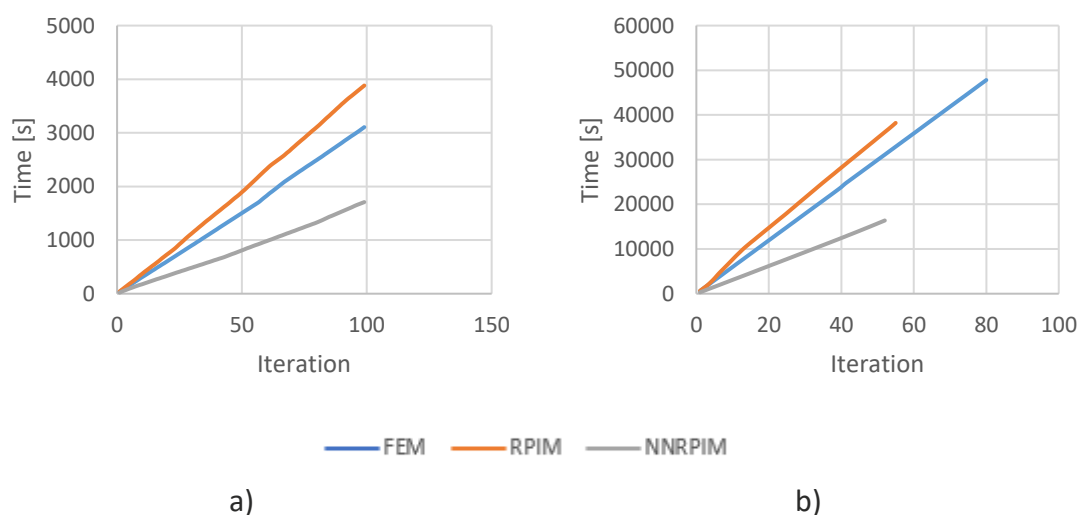


Fig. 40 - Computational time per iteration comparison between 2D and 3D models using FEM, RPIM and NNRPIM for a DR of 5%.

4.3.3 Proposed optimal topology design and structural analysis

Considering the solutions obtained from the structural optimization Table 8 and Table 9, two optimal designs are now proposed, Fig. 41. In these proposed designs, diagonal trabeculae were inserted in the optimal solutions in order to maintain only triangular shapes in the structure to confer more stiffness.



Fig. 41 – Proposed optimal design 1 (a) and 2 (b).

To evaluate the structural performance of the new designs, a structural analysis is performed between the original structure and the proposed designs. In Table 10 and Table 11 are presented the displacement and stress fields of the original and proposed designs, using FEM, RPIM and NNRPIM, for 2D and 3D models respectively. By observing these fields, it is possible to verify that the maximum displacement is obtained at the extremity of the handbrake where the force is applied, both for the original and for the proposed designs. As for the VM effective stress, higher stress concentrations occur for the proposed designs. In Table 12 and Table 13 are shown the results of the structural analysis performed on the original and proposed designs for 2D and 3D models respectively. As it was expected, higher displacement and VM effective stress values are obtained for the proposed designs. Thus, the proposed designs have a lower stiffness compared to the original. However, when divided the stiffness of the structure by its volume fraction, a structural gain is obtained for the optimized structures, achieving values around 30%. When comparing the displacement and VM effective stress obtained, between the different numerical methods they all get close values, with RPIM being the method to normally get higher values. Comparing the 2D and 3D models results, it is possible to verify that the values obtained from the 3D models are normally two times higher.

Table 10 – Displacement and stress fields of the original and proposed designs using FEM, RPIM and NNRPIM for 2D model.

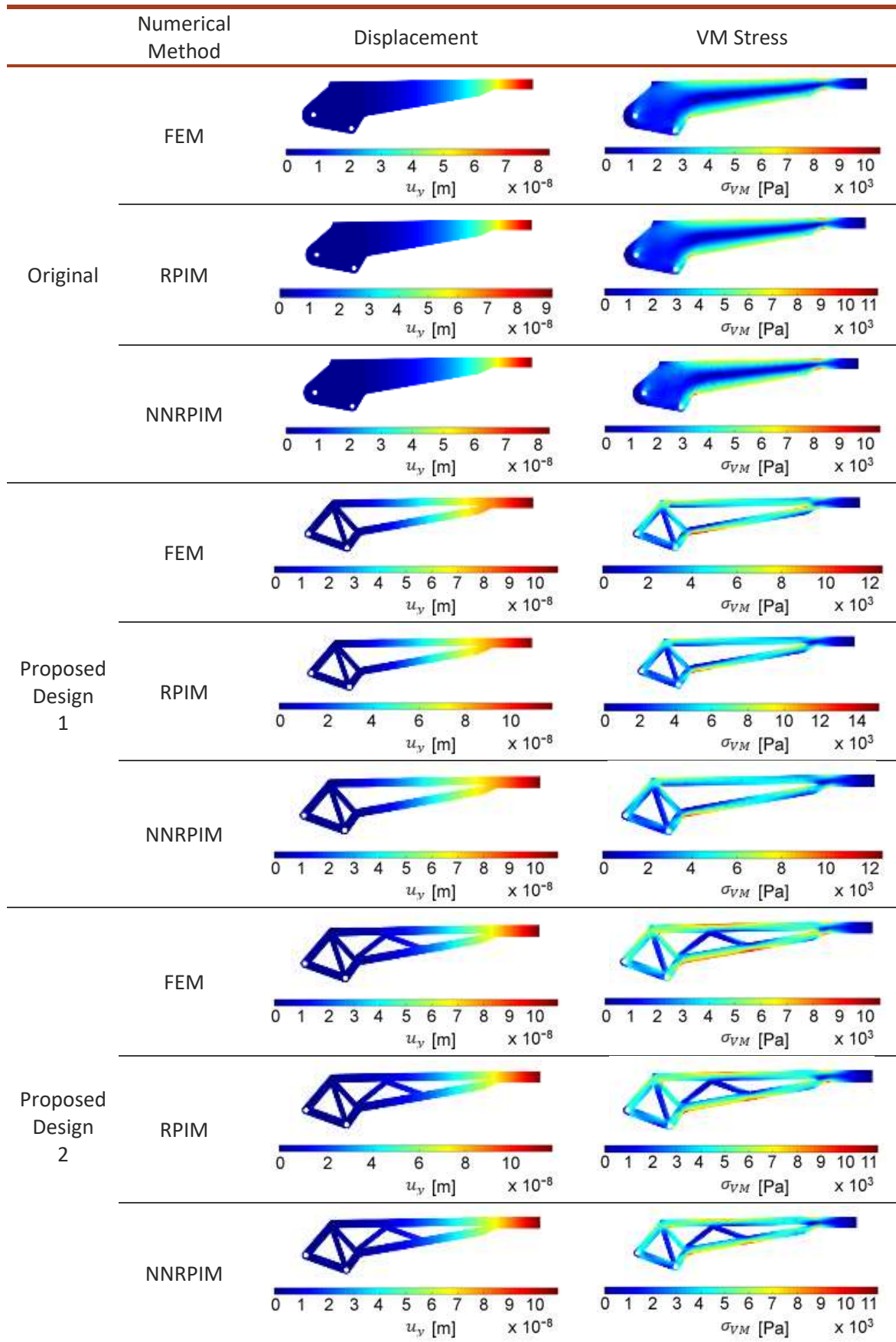


Table 11 - Displacement and stress fields of the original and proposed designs using FEM, RPIM and NNRPIM for 3D model.

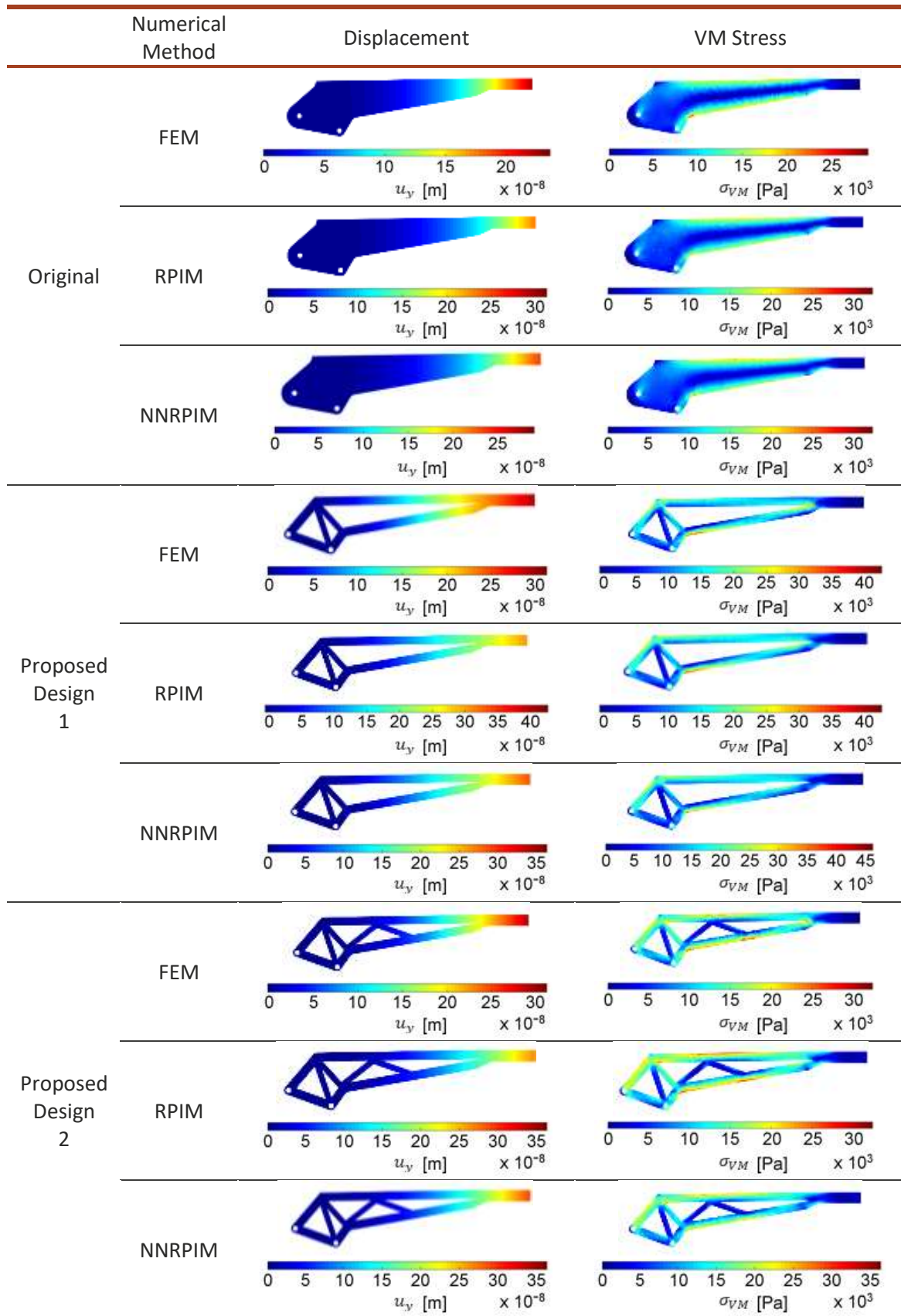


Table 12 – Structural analysis results for 2D model.

| | Original | | | Proposed design 1 | | | Proposed design 2 | | |
|--------------------------|-----------------------|-----------------------|-----------------------|------------------------|------------------------|------------------------|------------------------|------------------------|------------------------|
| | FEM | RPIM | NNRPIM | FEM | RPIM | NNRPIM | FEM | RPIM | NNRPIM |
| V_f | | 100 % | | | 61.25 % | | | 64.44 % | |
| $u_y^{max} [m]$ | 8.39×10^{-8} | 9.21×10^{-8} | 8.58×10^{-8} | 10.86×10^{-8} | 11.80×10^{-8} | 10.83×10^{-8} | 10.39×10^{-8} | 11.31×10^{-8} | 10.40×10^{-8} |
| $\sigma_{VM}^{max} [Pa]$ | 10.58×10^3 | 11.35×10^3 | 10.15×10^3 | 12.52×10^3 | 15.24×10^3 | 13.87×10^3 | 10.08×10^3 | 11.79×10^3 | 11.37×10^3 |
| $K [N/m]$ | 2.34×10^9 | 2.13×10^9 | 2.28×10^9 | 1.80×10^9 | 1.66×10^9 | 1.81×10^9 | 1.89×10^9 | 1.73×10^9 | 1.88×10^9 |
| $K/V_f [N/m]$ | 2.34×10^9 | 2.13×10^9 | 2.28×10^9 | 2.94×10^9 | 2.71×10^9 | 2.96×10^9 | 2.93×10^9 | 2.68×10^9 | 2.98×10^9 |
| Structural Gain | - | - | - | +25.64 % | +27.23 % | +29.82 % | +25.21 % | +25.82 % | +30.70 % |

Table 13 – Structural analysis results for 3D model.

| | Original | | | Proposed design 1 | | | Proposed design 2 | | |
|--------------------------|------------------------|------------------------|------------------------|------------------------|------------------------|------------------------|------------------------|------------------------|------------------------|
| | FEM | RPIM | NNRPIM | FEM | RPIM | NNRPIM | FEM | RPIM | NNRPIM |
| V_f | | 100 % | | | 61.25 % | | | 64.44 % | |
| $u_y^{max} [m]$ | 23.67×10^{-8} | 31.26×10^{-8} | 28.91×10^{-8} | 32.91×10^{-8} | 42.72×10^{-8} | 39.01×10^{-8} | 30.81×10^{-8} | 39.86×10^{-8} | 36.92×10^{-8} |
| $\sigma_{VM}^{max} [Pa]$ | 29.12×10^3 | 33.14×10^3 | 32.46×10^3 | 42.98×10^3 | 43.70×10^3 | 46.22×10^3 | 32.31×10^3 | 31.82×10^3 | 36.41×10^3 |
| $K [N/m]$ | 8.28×10^8 | 6.27×10^8 | 6.78×10^8 | 5.96×10^8 | 4.59×10^8 | 5.02×10^8 | 6.36×10^8 | 4.92×10^8 | 5.31×10^8 |
| $K/V_f [N/m]$ | 8.28×10^8 | 6.27×10^8 | 6.78×10^8 | 9.73×10^8 | 7.49×10^8 | 8.20×10^8 | 9.87×10^8 | 7.64×10^8 | 8.24×10^8 |
| Structural Gain | - | - | - | +17.51 % | +19.46 % | +20.94 % | +19.20 % | +21.85 % | +21.53 % |

CONCLUSIONS

5 CONCLUSIONS AND PROPOSALS OF FUTURE WORKS

In this work, the structural optimization was approached using meshless methods such as RPIM and NNRPIM and comparing to mesh-based method FEM.

Firstly, two benchmark examples reported in the literature were studied in order to validate the structural optimization process implemented in the software FEMAS. Thus, it was possible to determine how domain discretization, mesh and optimization parameters influence the optimization process.

After analysing the benchmark examples, considering the domain discretization, mesh and optimization parameters, the following conclusions were withdrawn:

- The usage of a uniformly distributed domain discretization significantly increases the achievement of good results;
- Refined meshes produce more detailed, smooth, and consistent solutions over sparser meshes;
- Under a combination of specific numerical method and domain discretization, using a DR of 2% and 3% it is possible to obtain optimal solutions. However, better and consistent results can be obtained for a DR between 4%, 5% and 10% with a higher variety of combinations;
- The higher the nodal density, the higher computational time per iteration;
- Normally between the numerical methods, NNRPIM takes more time per iteration following RPIM and FEM;
- Although the usage of higher DR reaches optimal solutions at earlier iterations, these tend to be coarse and less consistent.

Based on the conclusions withdrawn from the benchmark examples, a new structural optimization process was implemented, this time regarding an industrial application. Since the competition inside the automobile industry is increasingly higher, it becomes more and more important to increase the performance and efficiency of each part while granting a lower production cost. This is where the structural optimization plays a relevant role, because it can be applied to almost any kind of part and reduce its weight while granting the necessary mechanical properties to perform its function.

In this case a handbrake lever from a standard car was optimized reaching the following conclusions:

- Under specific combinations of parameters, both FEM, RPIM and NNRPIM were capable of reaching identical solutions;
- Based on the optimal solutions obtained, two proposed designs were developed and analysed, achieving mass reductions around 40% and not compromising the function of the part;
- Although good results have been achieved with 3D model, this analysis is inefficient since the computational time is much higher when compared with the 2D model;
- Despite higher displacements on the optimized models and therefore lower stiffness, when comparing the stiffness with the mass reduction, gains between 17% and 30% can be obtained.

Hereupon, it is possible to conclude that numerical meshless methods, despite having a higher computational time and required attention to the parameters imposed, can be a good alternative to the mesh-based numerical methods.

To conclude, it is important to highlight some difficulties and limitations that were felt throughout the development of the work. Due to nearly no background experience on how to work with the softwares used on this thesis, sometimes problems came up delaying the developed work. Since numerical methods require high computational costs, limitations on time and nodal mesh density had to be imposed, sometimes making it impossible to acquire smoother, detailed, and consistent solutions.

5.1 Future Works

Based on the work developed in this thesis, there are still some aspects that can be improved and studied in greater detail. The following future developments are then proposed:

- Further study of the optimization parameters would be necessary to obtain smoother and more consistent solutions;
- In order to validate the optimized solutions obtained, 3D models could be printed and tested;
- An automated process could be created for a better integration between the three softwares used;
- Improvements on FEMAS software could be made for better management of results and live visualization of these.

REFERENCES AND OTHER SOURCES OF INFORMATION

6 REFERENCES AND OTHER SOURCES OF INFORMATION

- [1] Y. Zhang, W. Ge, Y. Zhang, Z. Zhao, and J. Zhang, "Topology optimization of hyperelastic structure based on a directly coupled finite element and element-free Galerkin method," *Adv. Eng. Softw.*, vol. 123, pp. 25–37, 2018, doi: 10.1016/j.advengsoft.2018.05.006.
- [2] C. A. Felippa, "Introduction to Finite Element Methods - The Origins of the Finite Element Method," Boulder, 2004.
- [3] J. Belinha, A. L. Araújo, A. J. M. Ferreira, L. M. J. S. Dinis, and R. M. Natal Jorge, "The analysis of laminated plates using distinct advanced discretization meshless techniques," *Compos. Struct.*, vol. 143, pp. 165–179, May 2016, doi: 10.1016/j.compstruct.2016.02.021.
- [4] J. Belinha, *Meshless Methods in Biomechanics*, vol. 16. Porto: Springer International, 2014.
- [5] V. P. Nguyen, T. Rabczuk, S. Bordas, and M. Duflot, "Meshless methods: A review and computer implementation aspects," *Math. Comput. Simul.*, vol. 79, no. 3, pp. 763–813, 2008, doi: 10.1016/j.matcom.2008.01.003.
- [6] O. Askour, S. Mesmoudi, and B. Braikat, "On the use of Radial Point Interpolation Method (RPIM) in a high order continuation for the resolution of the geometrically nonlinear elasticity problems," *Eng. Anal. Bound. Elem.*, vol. 110, pp. 69–79, doi: 10.1016/j.enganabound.2019.09.015.
- [7] S. F. Moreira, J. Belinha, L. M. J. S. Dinis, and R. M. N. Jorge, "The anisotropic elasto-plastic analysis using a natural neighbour RPIM version," *J. Brazilian Soc. Mech. Sci. Eng.*, vol. 39, no. 5, pp. 1773–1795, 2017, doi: 10.1007/s40430-016-0603-x.
- [8] A. G. M. Michell, "LVIII. The limits of economy of material in frame-structures," *London, Edinburgh, Dublin Philos. Mag. J. Sci.*, vol. 8, no. 47, pp. 589–597, Nov. 1904, doi: 10.1080/14786440409463229.
- [9] M. P. Bendsøe and N. Kikuchi, "Generating optimal topologies in structural design using a homogenization method," *Comput. Methods Appl. Mech. Eng.*, vol. 71, no. 2, pp. 197–224, 1988, doi: 10.1016/0045-7825(88)90086-2.
- [10] S. Y. Wang, K. Tai, and M. Y. Wang, "An enhanced genetic algorithm for structural topology optimization," *Int. J. Numer. Methods Eng.*, vol. 65, no. 1, pp. 18–44, 2006, doi: 10.1002/nme.1435.
- [11] S. Bulman, J. Siens, and E. Hinton, "Comparisons between algorithms for structural topology optimization using a series of benchmark studies," *Comput. Struct.*, vol. 79,

- no. 12, pp. 1203–1218, 2001, doi: 10.1016/S0045-7949(01)00012-8.
- [12] Y. M. Xie and G. P. Steven, “A simple evolutionary procedure for structural optimization,” *Comput. Struct.*, vol. 49, no. 5, pp. 885–896, Dec. 1993, doi: 10.1016/0045-7949(93)90035-C.
- [13] O. M. Querin, G. P. Steven, and Y. M. Xie, “Evolutionary structural optimisation using an additive algorithm,” *Finite Elem. Anal. Des.*, vol. 34, no. 3–4, pp. 291–308, 2000, doi: 10.1016/S0168-874X(99)00044-X.
- [14] O. Querin, G. Steven, and Y. Xie, “Evolutionary structural optimisation (ESO) using a bidirectional algorithm,” *Eng. Comput.*, vol. 15, pp. 1031–1048, Dec. 1998, doi: 10.1108/02644409810244129.
- [15] H. E., “Fully stressed topological design of structures using an evolutionary procedure,” *Eng. Comput.*, vol. 12, no. 3, pp. 229–244, Jan. 1995, doi: 10.1108/02644409510799578.
- [16] A. Baumgartner, L. Harzheim, and C. Mattheck, “SKO (soft kill option): the biological way to find an optimum structure topology,” *Int. J. Fatigue*, vol. 14, no. 6, pp. 387–393, 1992, doi: 10.1016/0142-1123(92)90226-3.
- [17] M. Paley, M. Fuchs, and E. Miroshnik, “The Aboudi micromechanical model for shape design of structures,” Aug. 1996, doi: 10.4203/ccp.40.8.5.
- [18] Z. Juan, L. Shuyao, and L. Guangyao, “The topology optimization design for continuum structures based on the element free Galerkin method,” *Eng. Anal. Bound. Elem.*, vol. 34, no. 7, pp. 666–672, 2010, doi: 10.1016/j.enganabound.2010.03.001.
- [19] Z. L. Zhao, S. Zhou, K. Cai, and Y. Min Xie, “A direct approach to controlling the topology in structural optimization,” *Comput. Struct.*, vol. 227, pp. 106–141, Jan. 2020, doi: 10.1016/j.compstruc.2019.106141.
- [20] M. Golombic, *Algorithmic graph theory and perfect graphs*, 2nd ed. Amsterdam: Elsevier, 2004.
- [21] D. West, *Introduction to graph theory*, 2nd ed. Upper Saddle River: Prentice Hall, 1996.
- [22] J. A. Bondy and U. S. R. Murty, “GRAPH THEORY WITH APPLICATIONS NORfH-HOLLAND New York • Amsterdam • Oxford.”
- [23] H. Liu, Y. Tian, H. Zong, Q. Ma, M. Y. Wang, and L. Zhang, “Fully parallel level set method for large-scale structural topology optimization,” *Comput. Struct.*, vol. 221, pp. 13–27, Sep. 2019, doi: 10.1016/j.compstruc.2019.05.010.
- [24] M. Y. Wang, X. Wang, and D. Guo, “A level set method for structural topology optimization,” *Comput. Methods Appl. Mech. Eng.*, vol. 192, no. 1–2, pp. 227–246, Jan. 2003, doi: 10.1016/S0045-7825(02)00559-5.
- [25] G. Allaire, F. Jouve, and A. M. Toader, “Structural optimization using sensitivity

- analysis and a level-set method," *J. Comput. Phys.*, vol. 194, no. 1, pp. 363–393, Feb. 2004, doi: 10.1016/j.jcp.2003.09.032.
- [26] B. S. Morse *et al.*, "Interpolating Implicit Surfaces From Scattered Surface Data Using Compactly Supported Radial Basis Functions," in *Proceedings of the international Conference on Shape Modeling & Applications*, 2001, pp. 89–98, Accessed: Jan. 08, 2020. [Online]. Available: <https://scholarsarchive.byu.edu/facpub/572>This peer-reviewed article is available at BYU Scholars Archive: <https://scholarsarchive.byu.edu/facpub/572>.
- [27] S. Y. Wang, K. M. Lim, B. C. Khoo, and M. Y. Wang, "An extended level set method for shape and topology optimization," *J. Comput. Phys.*, vol. 221, no. 1, pp. 395–421, Jan. 2007, doi: 10.1016/j.jcp.2006.06.029.
- [28] H. Wendland, "Piecewise polynomial, positive definite and compactly supported radial functions of minimal degree," *Adv. Comput. Math.*, vol. 4, no. 1, pp. 389–396, Dec. 1995, doi: 10.1007/BF02123482.
- [29] B. Engineering, "Evolutionary structural optimization for problems with stiffness constraints," vol. 21, no. 1996, pp. 239–251, 2006.
- [30] M. H. Abolbashari and S. Keshavarzmanesh, "On various aspects of application of the evolutionary structural optimization method for 2D and 3D continuum structures," *Finite Elem. Anal. Des.*, vol. 42, no. 6, pp. 478–491, 2006, doi: 10.1016/j.finel.2005.09.004.

ANNEXES